Design and Application of Two Consistency Verification Model Methods for Weather Radar Networks in the South China Region

Heng Hu¹, Shunqiang Pei^{2*}, Lei Wu¹, Nan Shao¹, Chunyan Zhang³, Hao Wen¹, YunLei Liu¹

- ¹ Meteorological Observation Center of China Meteorological Administration, Beijing 100081, China;
- ² Public Meteorological Service Center, China Meteorological Administration, Beijing 100081, China;
- ³ Guangdong Meteorological Data Center, Guangzhou 510640, China;

Correspondence to: Shunqiang Pei (peishunqiangcma@163.com)

Abstract. The observational consistency between ground-based weather radars significantly impacts the quality of mosaic products and severe convection identification products. The real-time monitoring of observational biases between radars can provide a basis for calibration and validationadjustment. This study designed a consistency verification modelmethod for weather radar networks based on the FY-3G precipitation radar (SGRCM) and a ground-based weather radar network consistency verification modelmethod (AWRCM). From January to October 2024, observational experiments were conducted in the South China region involving 19 S-band weather radars and 13 X-band phased-array weather radars. The aim was to analyze the influencing factors of the consistency verification modelmethods and the observational biases of reflectivity factors for radars with different bands and systems. For the S-band weather radars, the difference in the mean bias between the two modelmethods ranged from -1.5 dB to 1.4 dB, and the difference in the mean standard deviation ranged from -1.2 dB to 1.2dB. For the X-band phased-array weather radars, the difference in the mean bias between the two modelmethods ranged from -6.67 dB to 0.84 dB, and the difference in the mean standard deviation ranged from -0.38 dB to 1.51 dB. The evaluation results of the two modelmethods show good consistency for weather radars with different bands. We selected one radar with a larger bias for recalibration and rectification, and the changes in bias before and after rectification thus provide a good indication of the improvement in network consistency among the radars.

1. Introduction

25

_Currently, there are 252 new-generation weather radars in operational use across mainland China (137 S-band and 115 C-band radars), with over 300 X-band weather radars. Except for certain mountainous and desert regions in the west, the new-generation weather radars cover most of the densely populated areas of the country. In regions with densely deployed radar sites, there are various degrees of overlap between neighboring radars. It has been observed that, over long-term operational use, radar reflectivity errors are influenced by factors such as an inadequate calibration of radar equipment parameters, beam blocking (Dinku et al., 2002; Liu et al., 2020), clutter interference, and electromagnetic interference in radar rainfall measurement (Travis et al., 2016; Tang et al., 2020; Zhang et al., 2003). These errors result in different observational outcomes from various radars for the same meteorological target due to influences such as the direction of the target, atmospheric conditions, attenuation, obstruction, and clutter. Echo intensity has always been an important parameter for identifying severe

convective weather, and it directly determines the accuracy of precipitation products estimated based on the Z-R relationship (Ryzhkov, A., et al.,1995; Fabry, F., et al.,1995; Steiner, M., et al.,1995; Bringi, V. N., et al.,2001). If adjacent radars observe echo intensity values with discrepancies within overlapping areas during the same observation period, it can affect the quality of radar network mosaics and increase uncertainty in the assimilation of radar data with other data sources. Therefore, it is crucial to perform a scientific, quantitative analysis of echo consistency in overlapping areas observed by neighboring radars in order to identify and correct observation biases. Some studies have proposed algorithms for evaluating the consistency between adjacent radars and provided a quality control method for matching points (Gourley et al., 2003; Smith, R., et al.,2018; Gao, J., et al.,2020). Zhang Zhiqiang et al. (2008) interpolated radar echoes into a three-dimensional grid to analyze the consistency in the positioning and echo intensity of four radars in the North China region. Vukovic et al. (2014) analyzed the impact of beam blockage in overlap regions between adjacent radars. Wu Chong et al. (2014) and Zhang Lin et al. (2018) conducted comparative studies on the echo differences in consistency between phased-array weather radars and new-generation Doppler weather radars. Xiao Yanjiao and Ye Fei et al. (2020a, 2020b) studied the echo intensity consistency along equidistant lines between adjacent radars based on quality-controlled CAPPI data. However, the CAPPI interpolation algorithm itself introduces biases, which can lead to uncertain sources of error in the network consistency analysis results (Lakshmanan, V., et al., 2006).

Using adjacent ground-based weather radars for a network consistency analysis can more easily identify observation biases in areas with dense radar deployment. However, in regions in the west with sparse radar stations, it may not be possible to match adjacent stations, thus necessitating the use of multi-source observational data for calibration, with precipitation satellite data being a commonly used reference standard. Internationally, the reflectivity factor deviations between satellite-borne precipitation radars, such as TRMM/PR (Tropical Rainfall Measuring Mission/precipitation radar) and GPM (Global Precipitation Mission) (Tropical Rainfall Measuring Mission/precipitation radar), and ground-based radars are used to correct radar reflectivity values (Wang et al., 20002009; Park et al., 2015; Warren et al., 2018; Protat et al., 2021; Zhi et al., 2023). Domestically, He Huizhong et al. (2002), Luo Bujian can et al. (2015), and Wang Zhenhui et al. (2015) compared the consistency between reflectivity measured using the TRMM precipitation radar and ground-based radar echo intensity in China.

50

60

However, the observational biases and stability of precipitation satellite data can also affect comparison results. Simply calculating quantitative biases between satellites and radars is not meaningful (Bolen, S. M., et al., 2003, Schwaller, M. R., et al., 2011). Using precipitation satellite data as a reference standard, transferring the systematic bias between ground-based weather radars and precipitation satellites to the results of a network consistency analysis for ground-based radars can help ascertain the observational biases of radars.

This study selects the South China region as the analysis area, where there is a rich variety of precipitation types and a wide distribution of multi-system and multi-band radars. Developing a multi-source integrated weather radar network consistency analysis modelmethod in this region will provide a solid basis for the method's promotion across China. We utilize observational data from China's independently developed FY-3G satellite, obtaining S/C/X-band reflectivity factors after quality control and frequency correction. During satellite overpasses, we perform spatiotemporal matching with ground-based

radars to match overlapping areas and analyze deviations. The satellite–ground comparison results are then integrated into the ground-based radar network consistency results to finally determine the reflectivity factor observation biases of the weather radars. This approach provides a quantitative, automated method for the calibration and adjustment of ground-based weather radars.

2. Materials and Methods

2.1 Data Introduction

The FY-3G satellite, part of the third batch of FY-3 satellites, was successfully launched on April 16, 2023, from the

Jiuquan Satellite Launch Center. The primary payload for precipitation measurement on this satellite is the PMR, which
includes both Ku- and Ka-band radars. This marks the first time China has achieved active satellite-based precipitation
detection, with the ability to obtain three-dimensional structural information within precipitation systems. Both radars employ
a fully matched scanning mode with a scanning angle of ±20 degrees. The spatial resolution at the nadir point is 5 km, and the
vertical resolution is 250 m. The design sensitivity is 18 dBZ for the Ku radar and 12 dBZ for the Ka radar (CMA,2023;

Wu,2023(a)).

This study utilizes Level 2 products from the FY-3G precipitation measurement radar, focusing primarily on the radar reflectivity factors for both the ascending and descending tracks of the Ku radar, corrected for frequency(Wu, et al., 2023(b)). These Level 2 products are provided in a latitudinal and longitudinal grid format ranging from the ground up to 20 km, with a data structure of nscan*nray*nbin. Here, nscan represents the variable number of scan lines, nray denotes the number of angle units per scan line, and nbin refers to the number of vertical range bins. Fig. 1 shows a brief overview of the descending orbit of the FY-3G precipitation satellite PMR Ku radar.

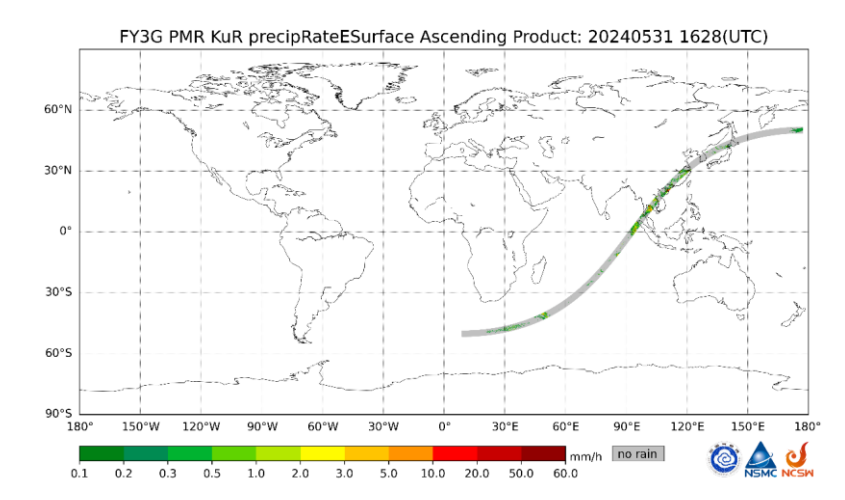


Figure 1. Brief overview of descending orbit of FY-3G precipitation satellite PMR Ku radar (cited from the National Satellite Meteorological Center, The satellite operates in a south-to-north direction.).

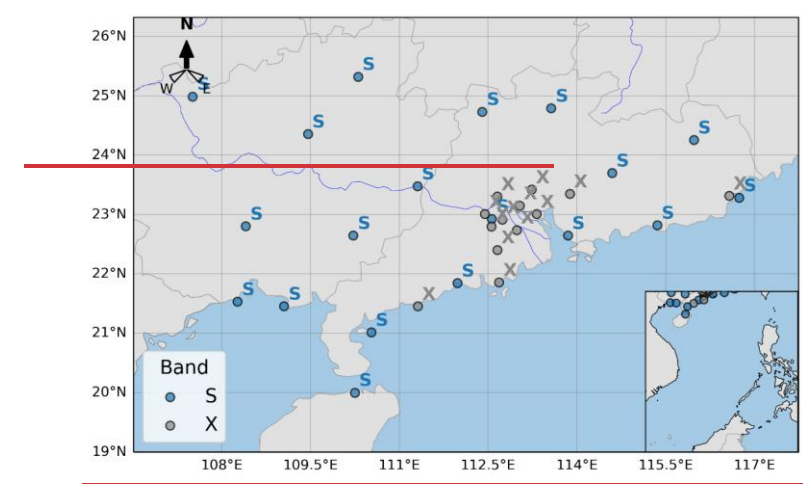
During the experiments, we used 19 S-band weather radars and 13 X-band phased array radars;. The distribution of the stations is shown in Fig. 2, and the specific hardware parameters are shown in Appendix Table 1A. The ground-based weather radars use standard-format base data. At present, the radars are undergoing mode-switching trials and will automatically switch observation modes according to real-time weather conditions: VCP (Volume Coverage Pattern)11 (for convective heavy precipitation), VCP21 (for stratiform precipitation), and VCP31 (for clear skies) (NWS, 2025). We selected 10 stations in the national S/C-band weather radar network to conduct a consistency analysis before and after mode switching. The evaluation results from 2024 show that mode switching has no significant impact on the method design involved in this study. The SGRCM method uses all elevation angle data from the radar, while the AWRCM method only uses the lowest 5 elevation angles, primarily to consider calculation efficiency.

90

100

Ground-based weather radars use standard format base data. Currently, the radars are undergoing mode-switching trials and will switch modes based on real-time weather conditions, utilizing VCP11 (for convective heavy precipitation), VCP21 (for stable precipitation), and VCP31 (for clear skies) modes (NWS,2025). Evaluation results from 2024 show that mode switching has no significant impact on the model design involved in this study. Full elevation angle data from the radar are used in the SGRCM. Meanwhile, only the lowest 5 elevation angles are used in the AWRCM, primarily to consider the efficiency of model calculations.

带格式的: 两端对齐



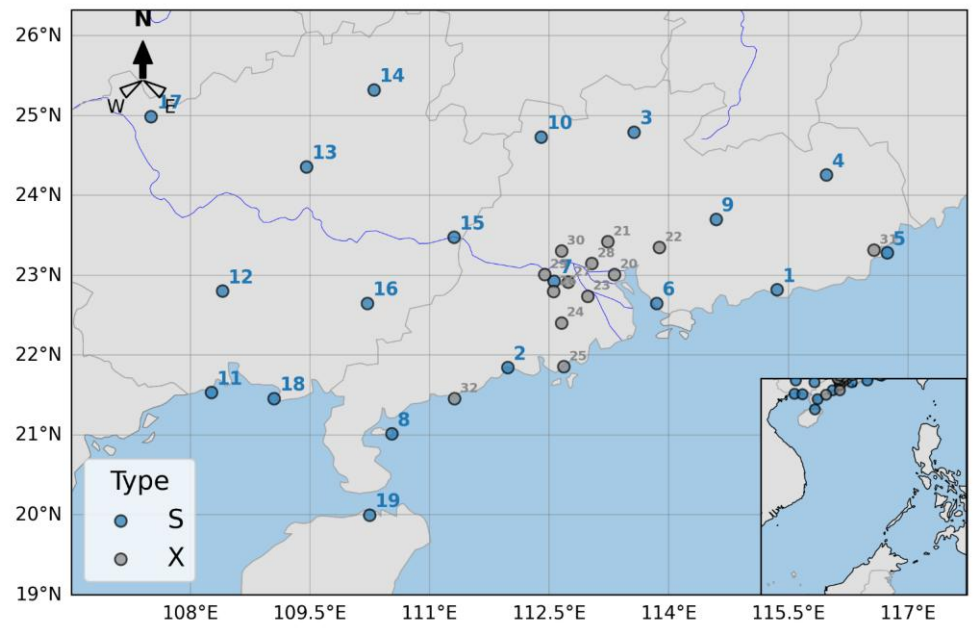


Figure 2, Distribution map of ground-based weather radar stations (Blue dots represent S-band weather radars, and gray dots represent X-band weather radars).

2.2 ModelMethod Introduction

110

130

140

2.2.1 Satellite and Ground-Based Radar Comparison ModelMethod (SGRCM)

First, the latitude and longitude data from the Geo_Fields module of the FY-3G Level 2 products are read, which represent grid points on the surface and at an 18 km altitude. Both layers consist of nscan*nray (3892*59) points. Using nbin as the step, the latitude and longitude for each grid point at every altitude level are calculated. The "height" from the PRE_(Data Preprocessing Module) module and the reflectivity factor Ze from the FRE_(Frequency Correction Module) module's "zFactorFrequencyCorrectionS" are also read, forming arrays of size 3892*59*400 (with a vertical sampling rate of 50 m). These data are then combined to obtain the satellite grid geographical information and reflectivity factor array.

The radar base data are read to generate a three-dimensional array of size m*n*k (where m represents the elevation angles, n represents the azimuth angles, and k represents the range bins). Coordinate system transformations are performed from polar coordinates to the first and second reference frames and, finally, to the geodetic coordinate system, which provides the latitude, longitude, and altitude for each range bin (Yang, et al.,2023), along with the reflectivity factor array. The steps for satellite—ground consistency comparison are as follows:

(1) Spatial and Temporal Collocation

Begin by identifying ground-based radars (GB) whose observational coverage significantly overlaps with the FY-3G PMR (SG) scanning region. Overlap criteria require that at least 3,000 (S/C-band) or 400 (X-band) PMR grid points fall within the GB's observation area. For temporal alignment, only data pairs where the observation times differ by less than 180 seconds are retained,

(2) Resampling

The FY-3G PMR Ku L2 product is a resampling dataset with 400 bins and a vertical resolution of 50 m, which differs from the original vertical resolution of 250 m used in the SG scanning mode. In this study, the data at each scanning track grid of SG are resampled into a four-dimensional (longitude, latitude, height, time) grid data with a vertical resolution of 250 m (80 bins) and a horizontal track resolution of 5 km, as the SG scanning mode shown in Fig. 3. That is, each SG grid is 5 km \times 5 km \times 250 m. Measurements that are too close to or too far away from the GB stations have significant errors. Through multiple experiments, this study selects the time-paired GB reflectivity data with a distance of 50-150 km away from the stations for S/C-band GBs and 9-42 km for X-band GBs. The GB reflectivity data are then transformed into three-dimensional (longitude, latitude, height) data.

(3) Extraction of Stratiform Rain Cases,

Stratiform precipitation is isolated using the precipitation classification provided by the SG product at each grid point. Both satellite and ground-based reflectivity values are further restricted to 20–35 dBZ within the 2–4 km altitude range to focus on relatively stable echoes.

(4) Pairwise Data Construction

设置了格式:字体:(中文) Times New Roman

设置了格式:字体: (中文) Times New Roman, 非加粗

带格式的: 居中, 缩进: 首行缩进: 0字符

设置了格式: 字体: (中文) +中文正文 (宋体), (中文) 简体中文(中国 大陆)

设置了格式: 字体: (中文) +中文正文 (宋体), (中文) 简体中文(中国 大陆)

设置了格式: 字体: (中文)+中文正文(宋体), (中文)简体中文(中国大陆)

设置了格式:字体:(中文)+中文正文(宋体),(中文)简体中文(中国 大陆)

For each spatial-temporal matchup, if multiple GB range bins correspond to a single SG grid cell, they are averaged to produce a composite GB reflectivity value. These paired values—SG and averaged GB reflectivity—form the basis for subsequent comparison.

(5) Consistency Assessment

145

When at least 20 such matched pairs are available, key statistical indices—namely bias, standard deviation, and correlation coefficient—are computed to quantitatively evaluate the consistency between the SG and the GB network. Satellite data have a relatively low horizontal resolution of 5 km by 5 km squares. For each square, the radar bins that fall within its latitude and longitude range are searched. The heights of the square grid points are compared with those of the radar bins, and a threshold is set (half of the radar range bin). The bins that are below this threshold are retained. In the radar base data, each radial has a 150 radial time, representing the observation time for all bins at that elevation and azimuth angle. The satellite observation time can be read from the Geo. Fields module and is accurate to the second. The times of the radar bins and satellite grid points are compared, retaining those within a specified threshold.

For each satellite grid point, all corresponding radar bins are averaged, and then the deviation, standard deviation, and correlation coefficient between the satellite Ze and the mean of the radar bins are calculated.

设置了格式: 字体: (中文)+中文正文(宋体), (中文)简体中文(中国

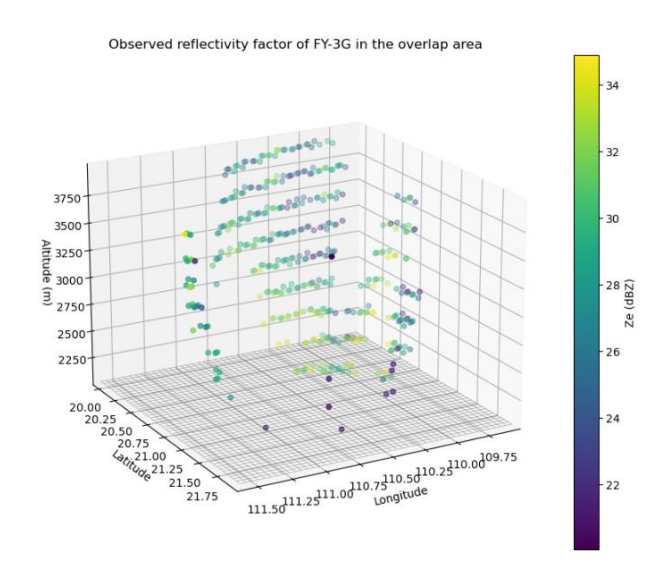
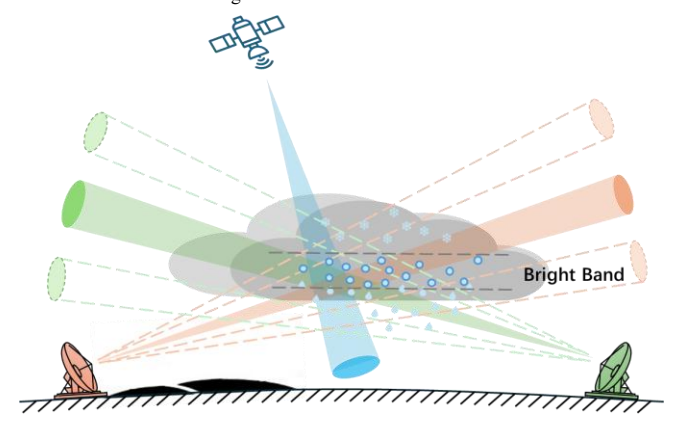


Figure 23. A comparison of the overlap region for the reflectivity factors observed by the FY-3G precipitation satellite and the ground-based S-band weather radar.



165

180

185

2.2.2 Adjacent Weather Radar Comparison Model Method (AWRCM)

The ground-based radar consistency algorithm selects base data from scans with inter-radar distances below a specified threshold (e.g., 300 km for S-band, 100 km for X-band) and volume scan intervals within 3 or 6 minutes, using elevation angles lower than 4.5 degrees from adjacent radars as the data source. Terrain data are used to remove occlusions, and non-precipitation echoes are filtered out. For spatial consistency matching, the horizontal and vertical distance thresholds are set to half the shorter path length among the radars; for temporal consistency, the difference in radial observation times must be below a defined threshold (e.g., 60 seconds). Observations with a signal-to-noise ratio less than 15 dB or insufficient horizontal filling at echo boundaries are excluded. The reflectivity threshold is set to 15–35 dBZ (with 35 dBZ serving as the S-band boundary between stratiform and convective precipitation echoes (Yu, 2007). Convective targets are excluded using vertically integrated liquid water (VIL>6.5 kg/m²). Finally, according to the 3-sigma rule, outliers in matched targets within overlapping radar regions are removed, and statistical metrics such as standard deviation and mean bias for the evaluation period are calculated to analyze consistency between adjacent radars.

Radars detect signals in a beam space, and adjacent radars have an overlapping radar beam coverage. Based on the spatial and temporal consistency of the same meteorological target points observed by the two radars, we refer to the overlapping target region as overlap points. These overlap points can be determined through precise calculations of geographic coordinates and radar coordinates, along with temporal consistency screening.

The spatial consistency matching technique constitutes the main challenge. Wu Chong et al. (2014) and Zhang Zhiqiang and Liu Liping (20132011) addressed the challenges of matching S-PAR-band phased-array weather radar data with new-generation weather radar data, which result from dissimilar spatial resolutions between the radars. They utilized polar-to-latitude-longitude coordinate transformations, reflectivity spatial interpolation, and other methods to design a spatial matching method for radar data with different resolutions and geographic locations. Zhang Lin et al. (2018) developed a method for the operational new-generation Doppler weather radars, where they transformed the polar coordinates of the first radar into latitude-longitude projection coordinates and searched for targets with consistent projections within the polar coordinates of the second radar. They set altitude thresholds to achieve the spatial matching of data from both radars.

The data addressed in this study pertain to the base data of the new-generation Doppler weather radars in operation. In the spatial matching algorithm, the above-mentioned methods are also employed. The process is described below. 带格式的: 缩进: 首行缩进: 2字符

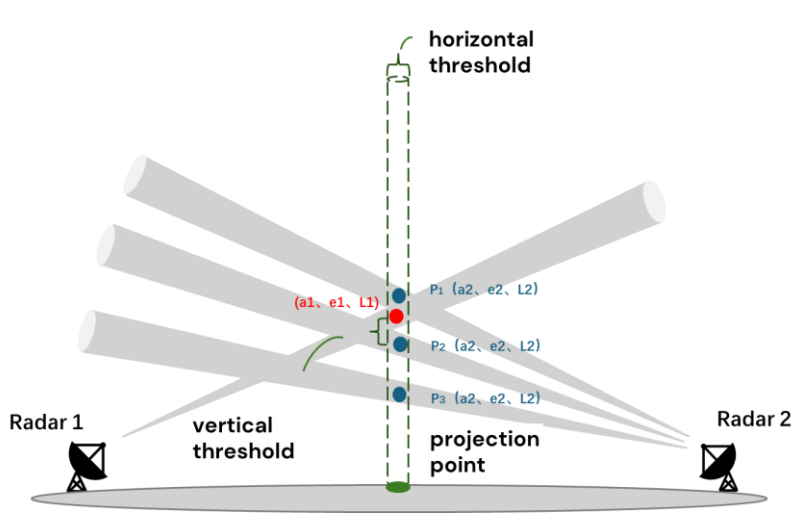


Figure 45. Schematic of two radars' spatial consistency algorithm.

As shown in Fig. 45, let the station coordinates of Radars 1 and 2 be (λ_l, ϕ_1, h_1) and (λ_2, ϕ_2, h_2) , respectively. For each volume scan data point from Radar 1, the polar coordinates—azimuth a_1 , elevation e1, and slant range L_1 (the red points in Fig. 45 are transformed into latitude, longitude, and altitude (λ, ϕ, H_l) using the formulas for converting radar polar coordinates to geographic coordinates and radar altitude calculations. The ground projection point's longitude and latitude are λ and ϕ . The formulas for these calculations are as follows, where $Km = \frac{4}{3}$ represents the effective Earth radius factor.

$$\varphi = \sin^{-1}(\cos\beta_1 \sin\varphi_1 + \sin\beta_1 \cos\varphi_1 \cos\alpha_1) \tag{1}$$

$$\lambda = \sin^{-1} \left(\frac{\sin a_1 \sin \beta_1}{\cos \varphi} \right) + \lambda_1 \tag{2}$$

 β_1 is the angle between the projection point and the center of the Earth at the location of Radar 1.

195

$$\beta_1 = K_m \tan^{-1} \left(\frac{L_1 \cos e_1}{Rm + h_1 + L_1 \sin e_1} \right) \tag{3}$$

Then, the formula for converting geographic coordinates to radar polar coordinates is used to calculate the data coordinates of Radar 2 under this projection. Radar 2 has multiple scanning elevation angles, and the scanning elevation angles e_2 for a data point is known. Using the coordinate transformation formula, it is straightforward to calculate the polar coordinates—azimuth a_2 , elevation e_2 , and slant range L_2 (the blue points in Fig. $4\underline{5}$, with the number of points determined by the intersecting radar 2 radial layers)—as well as their altitude h_2 , based on the conversion from geographic coordinates to radar polar coordinates.

$$\cos\beta_2 = \sin\varphi\sin\varphi_2 + \cos\varphi\cos\varphi_2\cos(\lambda_2 - \lambda) \tag{4}$$

设置了格式:字体:(中文)+中文正文(宋体),(中文)简体中文(中国大陆)

Here, β_2 is the angle between the projection point and the center of the Earth at the location of Radar 2. By using $\cos \beta_2$, $\sin \beta_2$ can be obtained; thus,

$$\sin a_2 = \frac{\cos \varphi \sin(\lambda - \lambda_2)}{\sin \theta_2} \tag{5}$$

Using Equation 1, $\cos a_2$ is obtained, and then the azimuth angle a_2 and slant range L_2 are calculated as follows:

$$a_2 = \operatorname{atan2}(\sin a_2, \cos a_2) \tag{6}$$

If $a_2 < 0$, then $a_2 = a_2 + 2\pi$.

210

215

220

225

230

235

$$L_2 = \frac{\tan\frac{R_2}{K_2}}{\cos e_2 - \sin e_2 \tan\frac{R_2}{k_2 m}} (Rm + h_2) \tag{7}$$

Rm is the equivalent Earth radius. After obtaining the target point polar coordinates for both radars, the altitude calculation formula is used to determine the target's elevation.

$$H = h + L\operatorname{sine} + \frac{L^2}{2Rm} \tag{8}$$

When the vertical height difference ΔH between the target point coordinates of the two radars is less than H_thre , where H_thre is the height difference threshold (Lu—et al.,2024), the spatial data coordinates are considered to be matched.

The temporal consistency requirement for overlapping points is that the observation times should be close. This time difference can be calculated by using the radar volume scan time or, more precisely, by using the radial scan time in the base data. Here, we first select time-close data using the radar volume scan time and then further filter based on the radial time.

After the base data from the two radars are matched in time and space, we obtain the reflectivity samples of the overlapping points. We refer to the difference in reflectivity (unit: dBZ) at the overlapping points between the two radars as the bias (unit: dB). The mean of the bias and the standard deviation are used as consistency evaluation metrics.

3.1 ModelMethod Accuracy Influence Factor Analysis and Processing

3.1.1 Spatial Matching

The horizontal resolution of the trajectory points of the FY-3G polar-orbiting satellite is 5 km, with a resampled vertical resolution of 50 m. As a result, the satellite grid centered on each trajectory point is treated as a flat grid, which significantly limits the number of radar range bins matched and sometimes results in no matches at all. To address this issue, the reflectivity data of the FY-3G polar-orbiting satellite at every 250 m height interval are selected for volume matching. This involves expanding the flat grid with a 50 m height to a larger grid with a 250 m height, allowing for more radar range bins to be matched and ensuring the statistical significance of the satellite and ground-based comparison results.

When matching satellite and ground-based data, it is important to consider the beam widening of weather radar at long distances, which can reduce the spatial geometric matching accuracy. Therefore, the satellite–ground matching distance range is set to 50-150 km. In terms of vertical height, to avoid the reduction in satellite product accuracy below clouds and the effects of the bright band, the height range is set to 2-4 km.

When analyzing the overlapping observation points of adjacent ground-based weather radars, excluding scenarios with obstructions, the distance between stations and the elevation difference between the radar sites are major influencing factors.

设置了格式:字体:(中文)+中文正文(宋体),(中文)简体中文(中国 大陆) Fig. 5-6 shows the three-dimensional distribution of the overlap region between two groups of radars. In group (a), the distance between the two radar sites is about 50 km, with an elevation difference of 278.8 m in the antenna feed height. In group (b), the distance between the two radar sites is nearly 200 km, with an elevation difference of 870 m in the antenna feed height. It can be observed that the smaller the distance and elevation difference, the more regular the distribution of the overlap points, with matched points distributed within the same elevation angle layer. As the distance and elevation difference increase, the distribution of overlap points becomes irregular, and the same elevation angle layer might match multiple elevation angle layers from the other radar. These analysis results indicate that it is not sufficient to simply select the midpoint between two radars as the overlap region; various factors such as the distance between stations and elevation differences must be considered.

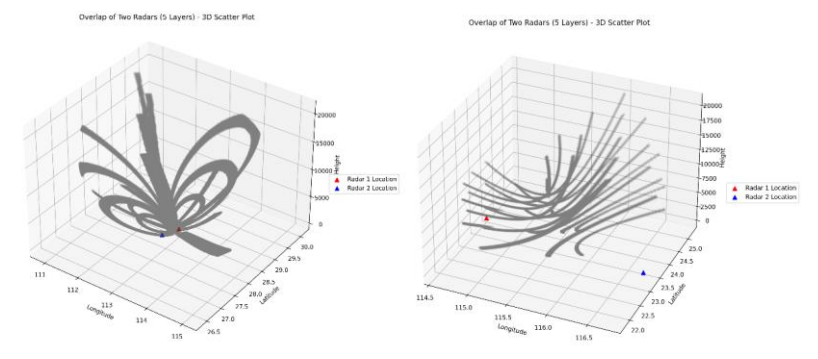


Figure 56. The impacts of distance between adjacent radar stations and elevation difference on the distribution of overlapping points.

3.1.2 Terrain blockage

240

245

When matching adjacent radars, severe terrain blockage in the direction of the overlap points for one of the radars may weaken the radar echo intensity. This can result in significant echo differences at the overlap points between the two radars, leading to inaccurate consistency evaluation results. This issue is not due to the radar itself (Maddox, R.A., et al., 2002; Bech J., et al., 2003).

Regarding terrain blockage, Liu Yunlei et al. (2020) utilized SRTM (Shuttle Radar Topography Mission) v4.1 digital elevation data to perform simulations and analyses of beam blockage for the new generation of operational weather radars in China. They sampled the radar detection range, calculated the latitude and longitude and detection height of target points based on radar station information, compared these to topographic data, and used radar altitude formulas and beam widening information to determine beam cross-section blockage at specific elevation angles. This provided beam blockage ratio data (hereinafter referred to as the obstruction rate) for each radar station.

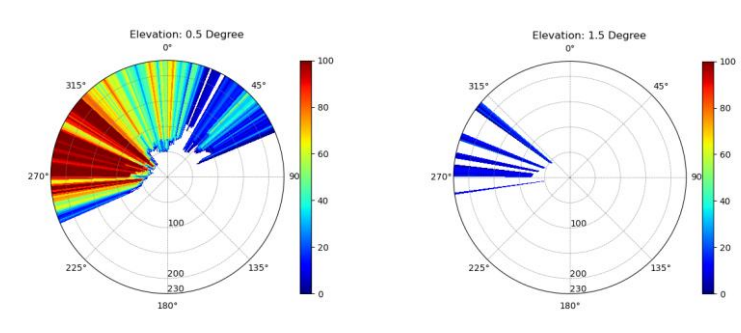


Figure 67. Terrain blockage at 0.5° and 1.5° elevation angles for Shantou S-band weather radar station in Guangdong. Figure 67 illustrates the terrain blockage at 0.5° and 1.5° elevation angles for Shantou station in Guangdong. The blockage is primarily distributed in the northwest direction of the station. When analyzing the observation bias between Shantou station and a neighboring radar located to its northwest, it is necessary to exclude the obstructed radials when calculating the overlap area, as doing so will reduce errors in the network consistency analysis.

3.1.3 Impact of Observation Targets

260

265

270

280

When the observation target is convective precipitation, the time threshold for calculating observation biases in the overlap areas between the satellite and ground-based radar needs to be limited to a very small range. However, this constraint may not provide a sufficient sample size for statistical analysis. In this study, the target was limited to stable stratiform precipitation, requiring the further classification of precipitation types. In satellite observation data, precipitation classification is performed using two methods: the vertical profile retrieval method and the horizontal pattern method. These methods classify precipitation into three categories: stratiform, convective, and other. The precipitation types identified by these two methods are then consolidated (Wu, 2023).

In the adjacent ground-based radar comparison verification modelmethod, we calculated the liquid water content for each grid point. Based on a statistical analysis, we set a threshold (Biggerstaff—M—I., et al., 2000; Xiao, et al., 2007) to classify observation targets into convective and stratiform precipitation. Fig. 7–8 shows a consistency comparison of two S-band weather radars (ID5 and ID8) in Guangdong before and after convective filtering. We adjusted the time threshold from 180s to 60s and set the vertically integrated liquid (VIL) threshold to 6.5 kg/m² (Xiao et al.,2009). After filtering, the number of matching points decreased, the correlation coefficient increased from 0.84 to 0.87, the standard deviation decreased from 4.68 dB to 4.34 dB, and the bias changed from -2.19 dB to -2.21 dB. It can be seen that increasing the radial time threshold and VIL filtering improved the correlation and standard deviation in the overlap regions of adjacent radars, although the bias slightly decreased. The reason for this requires further analysis with more accumulated samples.

设置了格式:字体:(中文)+中文正文(宋体),(中文)简体中文(中国大陆)

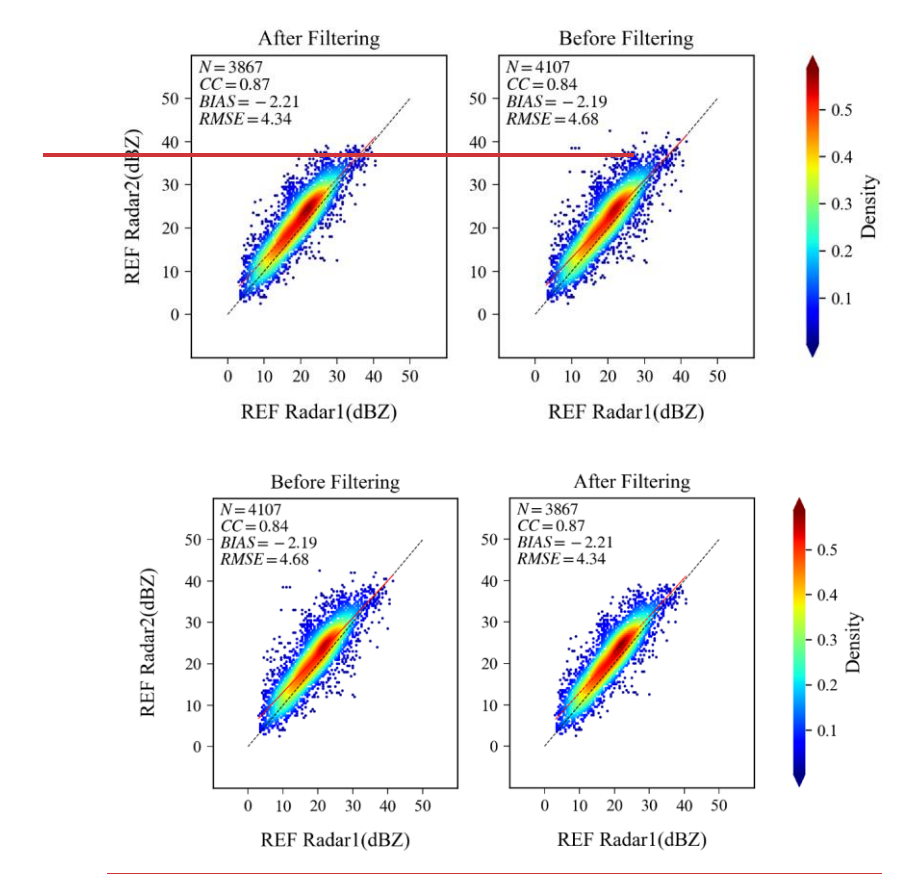


Figure 78. Comparison of two adjacent S-band radars before and after convective filtering: <u>left:(a) after before</u> filtering, (b) right: <u>before after</u> filtering.

3.1.4 Impact of Different Bands

285

BX5 is a standardized X-band weather radar. As a radar to be calibrated, it experiences co-channel interference when operated simultaneously with surrounding X-band radars, necessitating the creation of a blanking zone and the maintenance of its primary observation direction within the first quadrant. Approximately 2 km away from BX5, an S-band dual-polarization weather radar serves as a reference radar. Both radars can scan simultaneously to observe the same precipitation area.

设置了格式: 字体: (默认) Times New Roman, (中文) Times New Roman

带格式的: 缩进: 首行缩进: 2字符

Figure 8-9 shows the reflectivity factors observed at a 0.5-degree elevation angle by the two adjacent S/X-band weather radars around 14:35 on May 26, 2024, with the X-band radar data not corrected for attenuation.—The white box in the figure identifies the same echo region. In panel (a), the reflectivity factor observed by the X-band radar is 10-15 dBZ weaker than that in panel (b) observed by the S-band radar. A probability distribution analysis of the reflectivity factors from the overlapping observation areas of the two radars is conducted, as shown in-on the left side of Fig. 8910. The calculated bias, standard deviation, and correlation coefficient are -6.74 dB, 10.12 dB, and 0.18, respectively. We applied an adaptive attenuation correction method (Testud et al.,2000(a)) to the BX5 radar, and then analyzed the bias between the corrected data and that from the adjacent S-band weather radar. The bias was reduced to -1.68 dB. The X-band radar shows significant attenuation in strong echo areas (Testud Testud, J., et al.,2000(b); Bringi et al., v. N., 2001). Therefore, in subsequent analyses of the network consistency between X-band and other band weather radars, the reflectivity factor range is set (e.g., 15-35 dBZ), with certain limitations also applied to the signal-to-noise ratio.

300

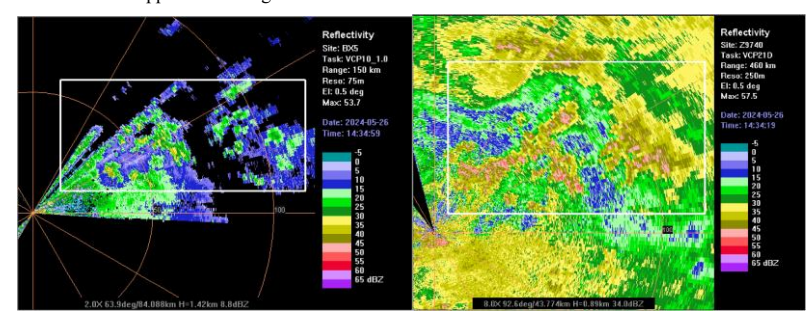


Figure 89. Comparison of reflectivity factors observed by adjacent SX-band (left) and XS-band (right) weather radars during a precipitation event on May 26, 2024, at 14:35.

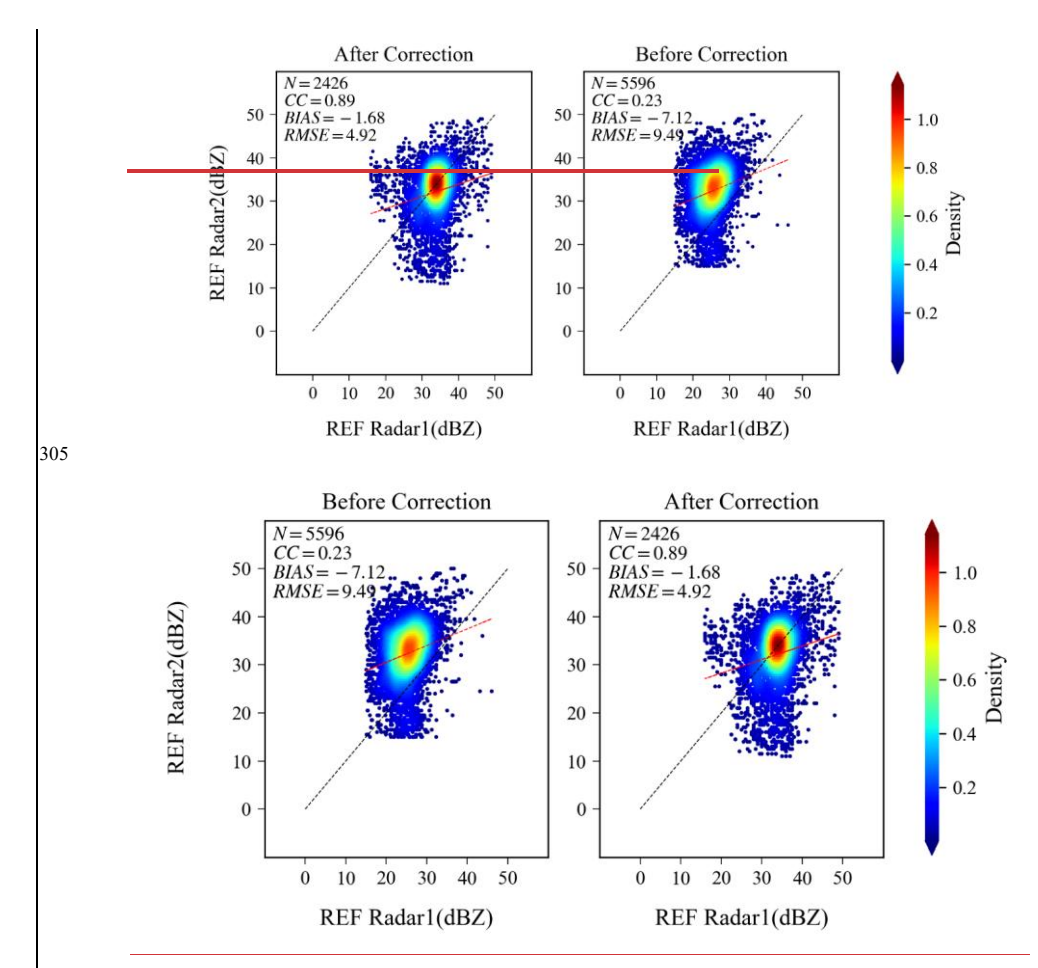


Figure 910. Analysis results of reflectivity bias in the overlapping observation area of adjacent SX- and XS-band weather radars on May 26, 2024, at 14:35 (the horizontal axis (Radar1) represents the X-band radar, while the vertical axis (Radar2) represents the S-band radar).

3.1.5 Impact of Non-Meteorological Echoes

310

In radar consistency evaluation algorithms, the impact of non-meteorological echoes at overlapping points must be considered. These echoes may be caused by noise or insufficient target filling, among other reasons. Coastal stations are often

带格式的: 缩进: 首行缩进: 2字符

affected by changes in atmospheric refractivity over the ocean (Melsheimer, C., et al., 1998; Skolnik et al., M. I., 2008), leading to clear-air echoes or sea clutter, which can significantly influence the comparison results of overlapping areas between adjacent radars.

315

320

325

As illustrated in Fig. 1011, the two weather radar stations are coastal stations in South China, with an observation time difference of about 2 minutes and a distance of approximately 140 km between them. In panel (a), the third and fourth quadrants exhibit clear-air echoes, while in panel (b), these quadrants display sea clutter echoes. When performing overlap area matching, consistency calculations were conducted for these non-precipitation echoes, resulting in a bias of 8.84 dB. This bias clearly does not stem from radar hardware performance. Therefore, when analyzing the comparison results of overlapping areas between adjacent weather radar stations, it is crucial to first exclude non-precipitation echoes in order to minimize their impact on the statistical outcomes.

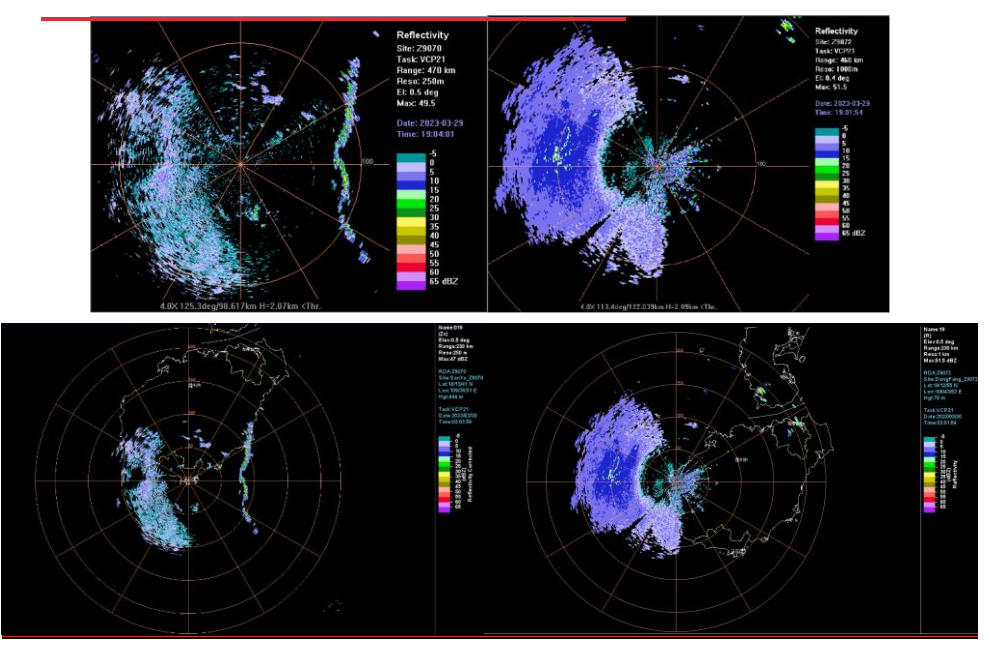


Figure 1011. Impact of clear-air echoes and sea clutter on overlapping area comparison analysis at coastal weather radar stations.

To mitigate the impact of noise on the evaluation results, we improved our method by filtering based on the signal-to-noise ratio (SNR), excluding target points with an SNR below a certain threshold (set here to 15 dB). To calculate the degree of filling, we considered horizontal filling (Kitchen, M., et al., 1993; Doviak, et al., 2006). Typically, target points at the edges

335

of echoes have a lower degree of filling. We used the reflectivity standard deviation (Ref SD) of the radar echo compared to that of the surrounding points to represent the degree of incomplete horizontal filling of reflectivity (as shown in Fig. 4412. The larger the reflectivity standard deviation value, the lower the degree of adequate horizontal filling. By removing points with a reflectivity standard deviation greater than a specified threshold (set here to 12 dB), we could eliminate target overlapping points at the edges of echoes with incomplete horizontal filling.

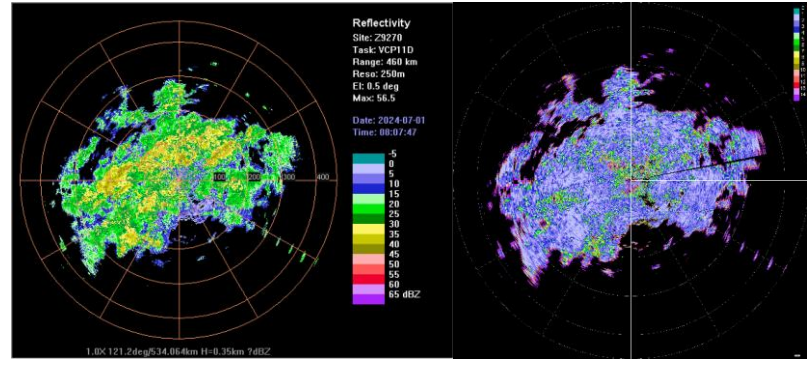
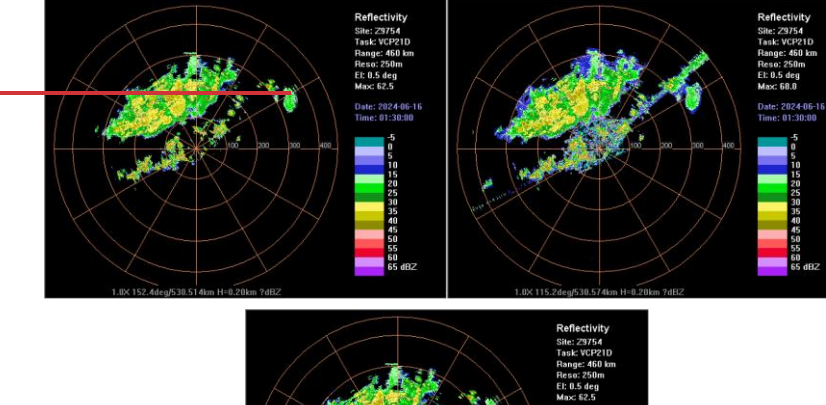


Figure 1112. Schematic of the degree of beam incomplete filling (The right side of the figure shows the Ref SD results (unit: dB), with a ring set every 100 km and the outermost ring at 460 km.).

Electromagnetic interference can affect the quality of weather radar observation data and the reflectivity factor comparison results between radars (Saltikoff, E., et al., 2016; Nguyen, L., et al., 2017). Fig. 42-13 (left) shows radial interference occurring at an elevation angle of 0.5 degrees between radial angles of 45 and 52 degrees on the Shantou weather radar (ID5) in Guangdong at 01:30 (UTC) on June 16, 2024. By using a fuzzy logic method(Wen et al., 2020) to eliminate the radial interference, a quality-controlled reflectivity factor map was obtained, as shown in Fig. 12-13 (right). A consistency analysis comparing the reflectivity before and after interference removal with that of a nearby S-band weather radar showed that the correlation coefficient, bias, and standard deviation of the two radars improved from 0.88, -1.70 dB, and 4.97 dB to 0.89, -345 1.68 dB, and 4.92 dB, respectively. This indicates that radial interference reduces the observation consistency between adjacent radars.

设置了格式: 字体: 非加粗



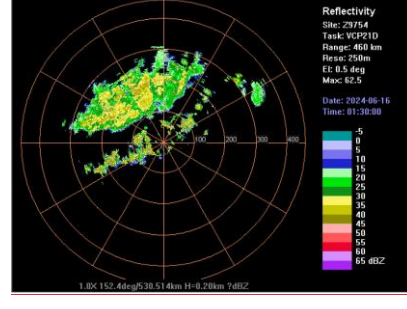


Figure 1213. Reflectivity factor at a 0.5-degree elevation angle for the Guangdong Shantou radar before and after electromagnetic interference quality control: (left) before quality control; (right) after quality control.

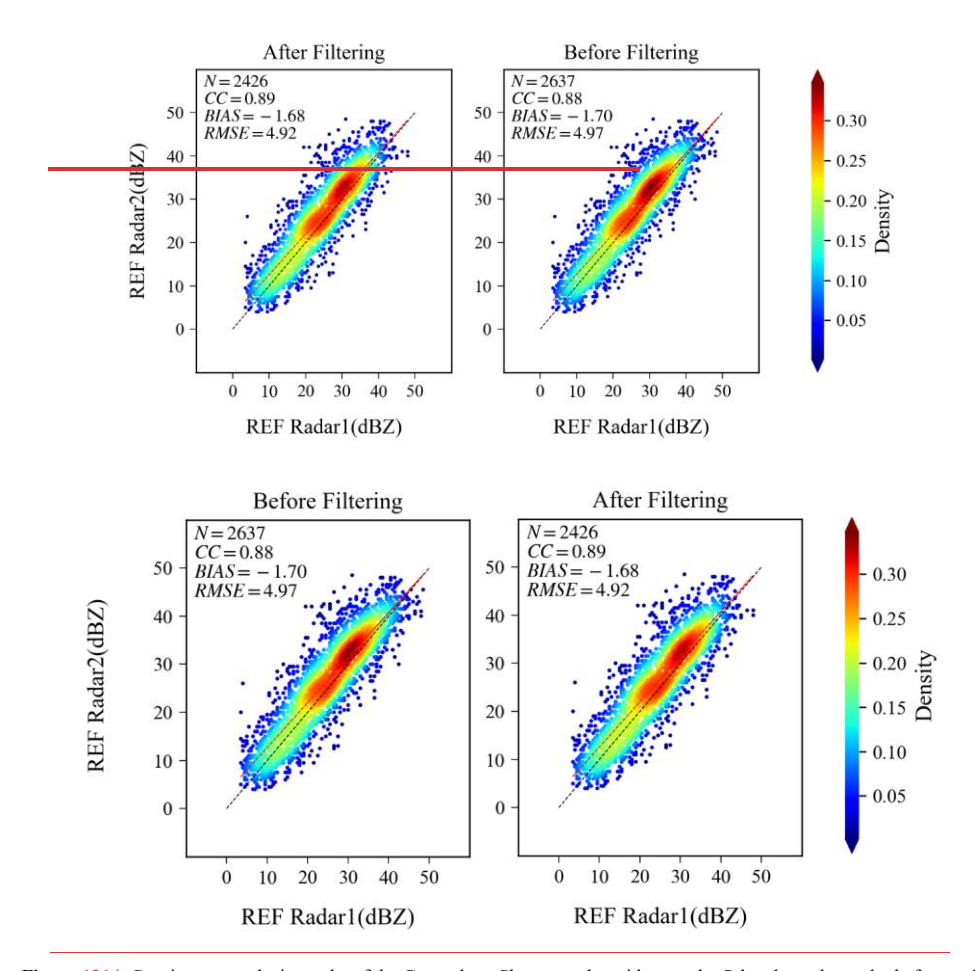


Figure 1314. Consistency analysis results of the Guangdong Shantou radar with a nearby S-band weather radar before and after electromagnetic interference quality control. (Radarl is the ID5, and Radar2 is ID8)

3.2 Regional Experimental Results

355

3.2.1 Evaluation Results of the S-band

In the ground-based consistency analysis, we set a distance threshold between neighboring radars (for example, 200 km for S-band radars). Any two radars within this threshold can be paired for comparison. Taking Radar 1 as an example, if it can

带格式的: 缩进: 首行缩进: 2字符

be paired with n surrounding radars, then each volumetric scan will yield n sets of comparison results, and the average of these n results is taken as the final consistency bias value for Radar 1 at that time. If a particular radar has a large systematic bias, this will be reflected in the bias average. A large standard deviation indicates that the radar's observation results are more dispersed, suggesting a need for further calibration. From January to October 2024, 19 S-band new-generation weather radars in South China were selected to conduct both ground-based and satellite-to-ground consistency analyses. The differences between the two methods were evaluated using bias and standard deviation as metrics. Fig. 14-15 presents the bias comparison results from both methods. The bias trends are generally similar, with the ground-based consistency analysis showing bias values ranging from -2.06 to 1.65 dB, and a mean of -0.12 dB. The satellite-to-ground consistency analysis produces bias values ranging from -1.28 to 1.13 dB, with a mean of -0.01 dB; notably, the absolute bias is smaller for the satellite-to-ground method than for the ground-based method. Fig. 15-16 shows the standard deviation comparison for the two methods, mainly concentrated below 4 dB. The differences between the two standard deviations are within ±1.2 dB, indicating that both methods provide relatively close assessments of the dispersion of ground-based radar observation bias.

360

365

370

Figure $\frac{45-16}{2}$ shows a comparison of the standard deviations between the two methods, which are mainly distributed below 4 dB. The differences between the two results are within ± 1.2 dB. It can be seen that the two methods provide relatively consistent evaluations of the dispersion of biases in ground-based radar observations.

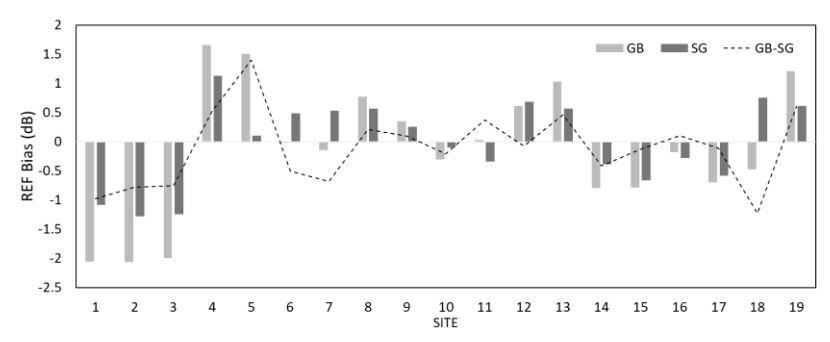


Figure 1415. Comparison of mean bias between ground-based and satellite–ground consistency for S-band weather radars in the South China region.

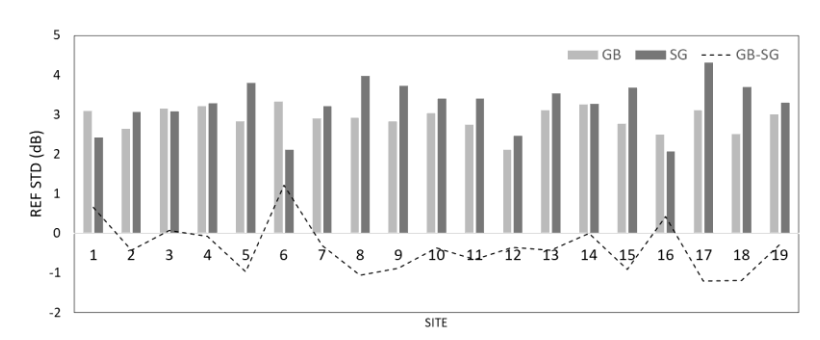


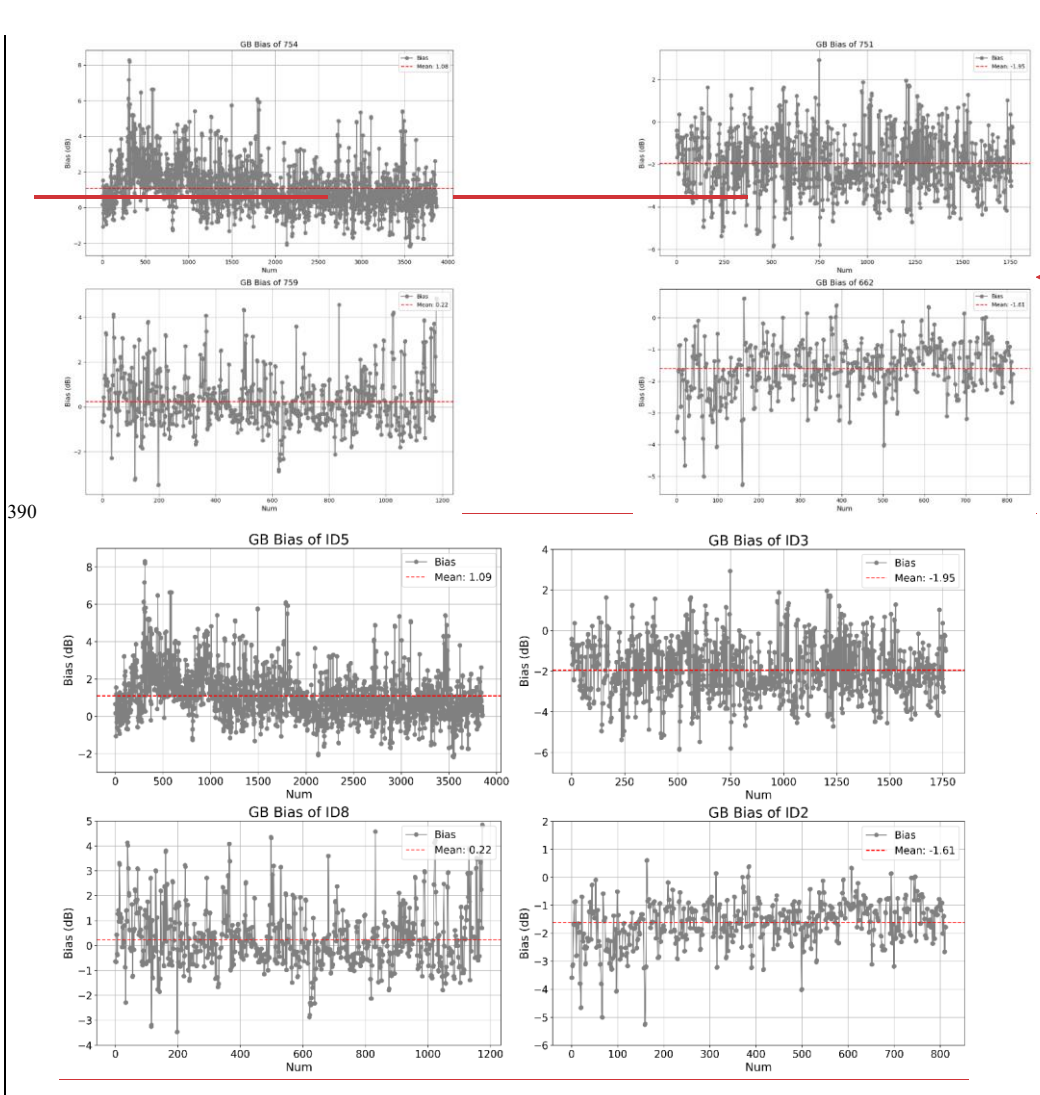
Figure 1516. Comparison of standard deviations between ground-based and satellite—ground consistency for S-band weather radars in the South China region.

380

Data from four selected stations were analyzed. Fig. <u>16-17</u> shows the bias analysis results for ground-based consistency. The gray dots represent the bias of individual observation times, while the red dashed line represents the mean bias. Due to differences in the number of neighboring stations matched and the weather processes involved, the sample size for analysis varies. The mean bias between stations 754, 759, and their neighboring stations is greater than 0, indicating that these two radars are relatively stronger in the ground-based network, with station 754 showing a particularly noticeable positive bias. In contrast, stations 751 and 662 exhibit weaker biases.

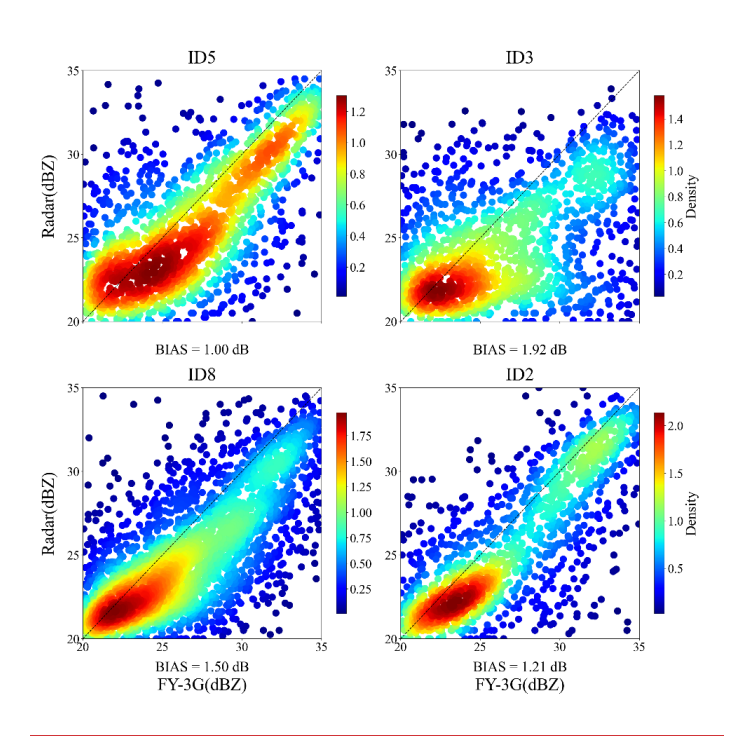
Figure <u>17-18</u> shows the satellite–ground comparison results for the four stations. It can be observed that the reflectivity factor of the FY-3G PMR is generally <u>strongerlarger</u>. Among the four stations, station 754 has the smallest bias, which is relatively consistent with the results of the ground-based analysis.

设置了格式: 字体: (默认) Times New Roman, (中文) Times New Roman



带格式的: 两端对齐

Figure 1617. Bias analysis results of ground-based consistency for individual S-band weather radar stations.



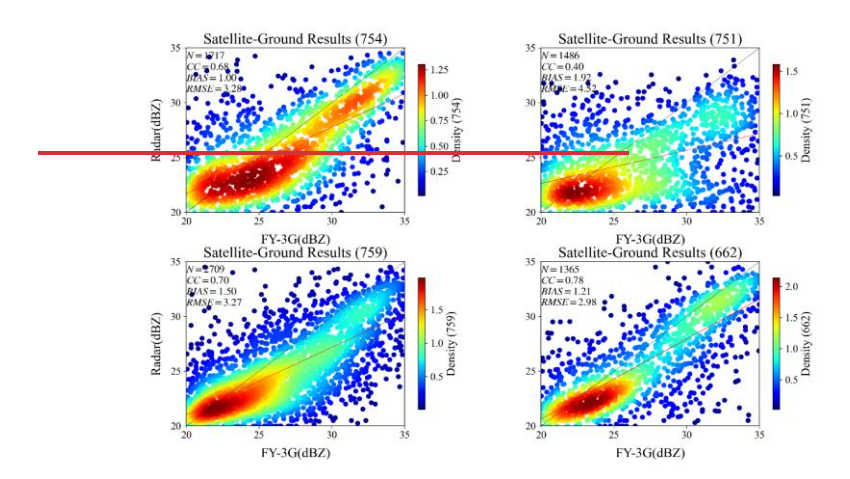


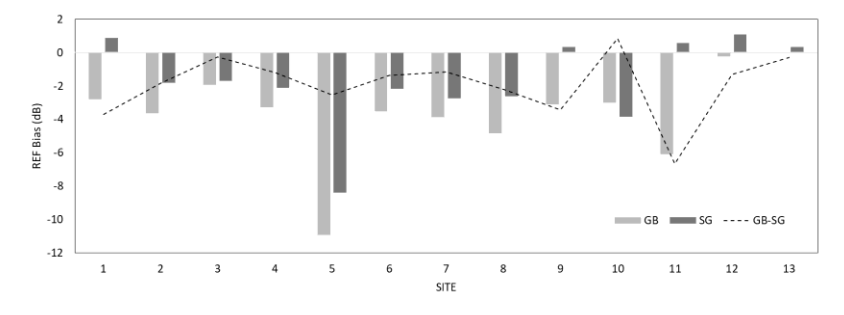
Figure 1718. Satellite–ground consistency analysis results for individual S-band weather radar stations.

3.2.2 Evaluation Results of X-Band Phased-Array Radars

395

400

Ground-based and satellite—ground consistency analyses were conducted for 13 X-band phased-array weather radars in Guangdong Province, for which attenuation correction has already been applied to the base data (Xiao et al.,2021). The bar chart in Fig. 18-19 represents the distribution of the mean bias for the two methods. For most phased-array radars, the average bias of both the ground-based and satellite—ground consistency is less than 0, indicating that the reflectivity of the phased-array radars is relatively weaker. The dashed line represents the difference between the ground-based consistency bias and the satellite—ground consistency bias. The results are mainly distributed below 0, suggesting that the bias results from the ground-based analysis are relatively larger.



带格式的: 缩进: 首行缩进: 2 字符

Figure 1819. Comparison of mean bias between ground-based and satellite—ground consistency for X-band phased-array weather radars in the South China region.

The bar chart in Fig. 19-20 represents the distribution of the standard deviations of the two analysis methods. The results of the ground-based analysis range from 3.15 to 3.95 dB, while those of the satellite–ground analysis range from 1.96 to 4.01 dB, with larger differences in standard deviation observed between different radars in the satellite–ground analysis. The dashed line represents the difference between the two analysis results, with most results distributed above 0 dB, indicating that the ground-based analysis results are relatively larger.

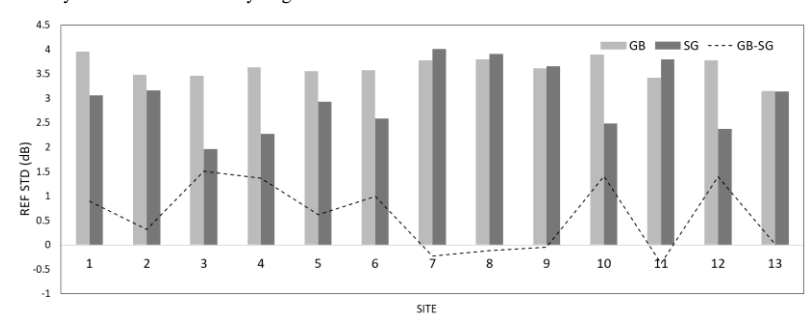
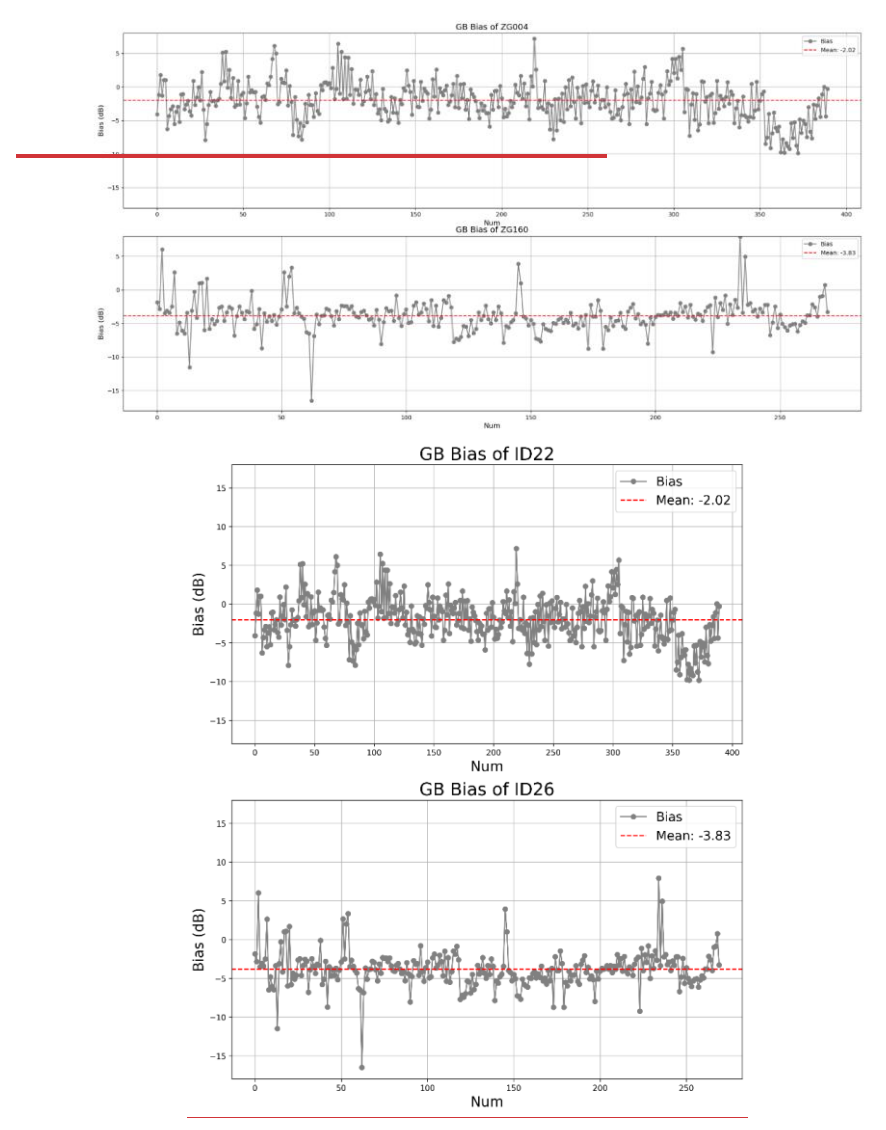


Figure 1920. Comparison of standard deviations between ground-based and satellite—ground consistency for X-band phasedarray weather radars in the South China region.

Two X-band phased-array weather radars, 004 and 160, were selected for analysis. Fig. 20-21 shows the bias analysis results for the ground-based consistency. The gray dots represent the bias of individual observation times, while the red dashed line represents the mean bias. It can be observed that the differences in overlapping observation points between the phased-array weather radars and the surrounding S-band weather radars are mainly distributed below 0. The mean biases are -2.02 dB and -3.83 dB, respectively, indicating that the X-band phased-array radars are weaker than the S-band solid-state weather radars.



 $\textbf{Figure } \textcolor{red}{\textbf{2021}}. \textbf{ Ground-based consistency bias analysis results for individual X-band phased-array weather radars.}$

Figure 21-22 shows the satellite—ground consistency analysis results for the two radars. The bias in the figure represents the reflectivity factor of the phased-array radar minus that of FY-3G, with values of 1.66 dB and 2.11 dB, respectively. This also indicates that the reflectivity factor observed by the X-band phased-array radars is weaker, but the bias results are smaller than the ground-based analysis results. The satellite—ground standard deviation of radar 004 is smaller than that of radar 160. From the bias distribution of overlapping observation points, it can be seen that the satellite—ground bias of radar 160 exhibits greater dispersion.

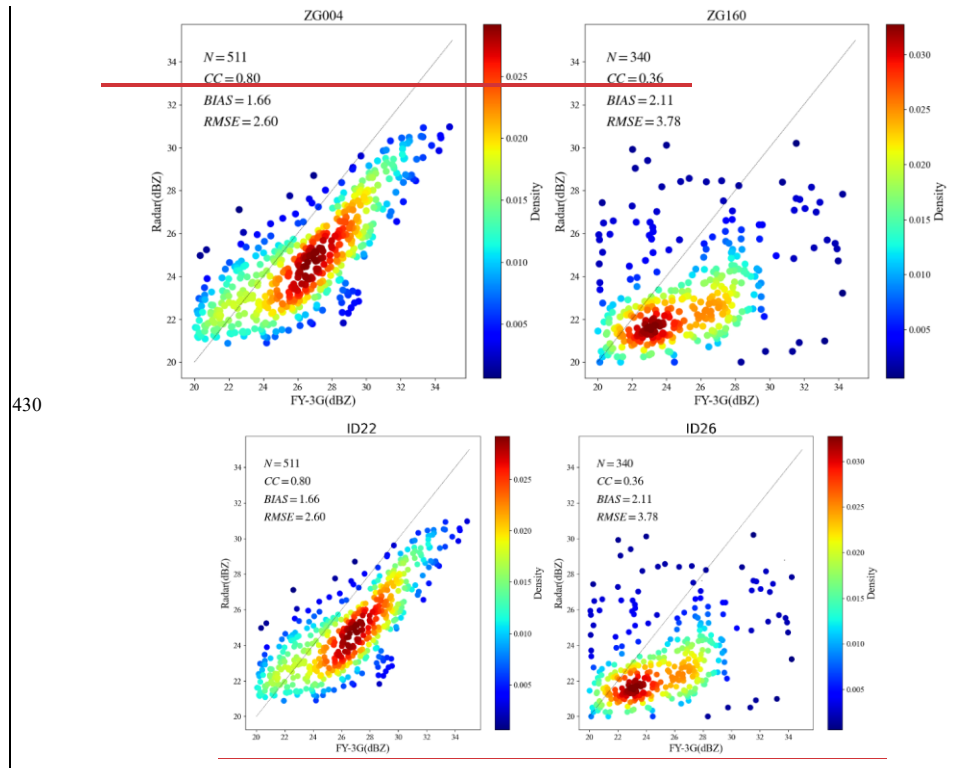


Figure 2122. Satellite–ground consistency bias analysis results for individual X-band phased-array weather radars. **4. Discussion**

In daily operations, the two consistency evaluation methods provide a basis for real-time monitoring of observational biases in ground-based radars. Once a significant change is detected in the consistency evaluation results, we will initiate the subsequent calibration procedures, including Solar Calibration (Holleman; et al., 2022) and Metal Sphere Calibration (Ao, et

带格式的: 缩进: 首行缩进: 2 字符

设置了格式: 字体: (默认) Times New Roman, (中文) Times New Roman al., 2022). To determine whether the results of the above consistency analyses are correct and whether they can provide a basis for calibration, we conducted a rectification experiment using an SC (a model of S-band radar) -modelmethod weather radar located in Sanya City, Hainan Province. Before calibration, the deviation between this radar and surrounding radars and that between satellite and ground measurements both exceeded 2.7 dB. During the system calibration, the system parameters of each radar station were revised and recalibrated. The main adjustment involved modifying the transmission branch feeder loss parameter, changing the single-H transmission feeder loss from 1.59 dB to 2.50 dB. By calibrating the internal continuous-wave power using the external continuous-wave power, the internal continuous-wave power before the low-noise amplifier was adjusted from 0.30 dBm before rectification to 1.30 dBm.

440

445

450

Figures 2223-23-24 show the ground-based consistency results and satellite—ground consistency results before and after calibration, indicating that the deviation was reduced to below 2.5 dB. The deviation in the satellite—ground comparison decreased from 4.58 dB to 1.97 dB. However, the stability of the rectification still requires further verification through the accumulation of long-sequence data.

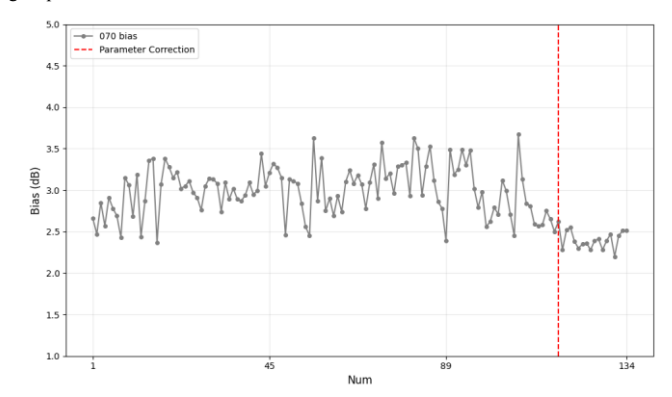


Figure 2223. Ground-based consistency results of the SC modelmethod radar in Sanya City, Hainan Province, before and after rectification. The gray line in the chart represents the variation in deviation, while the red dashed line indicates the rectification time.

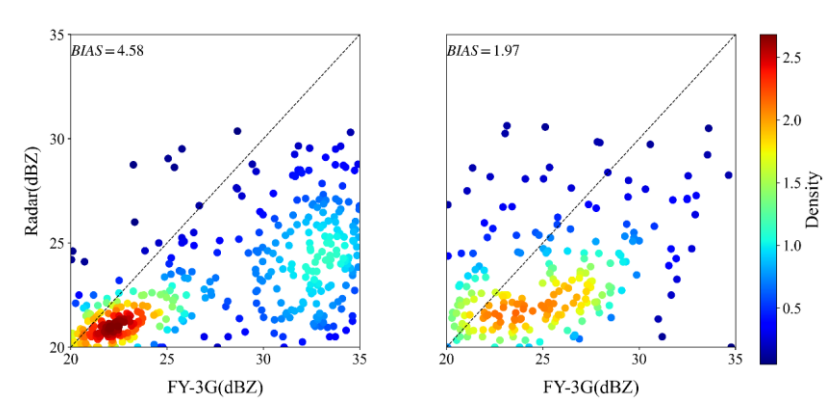
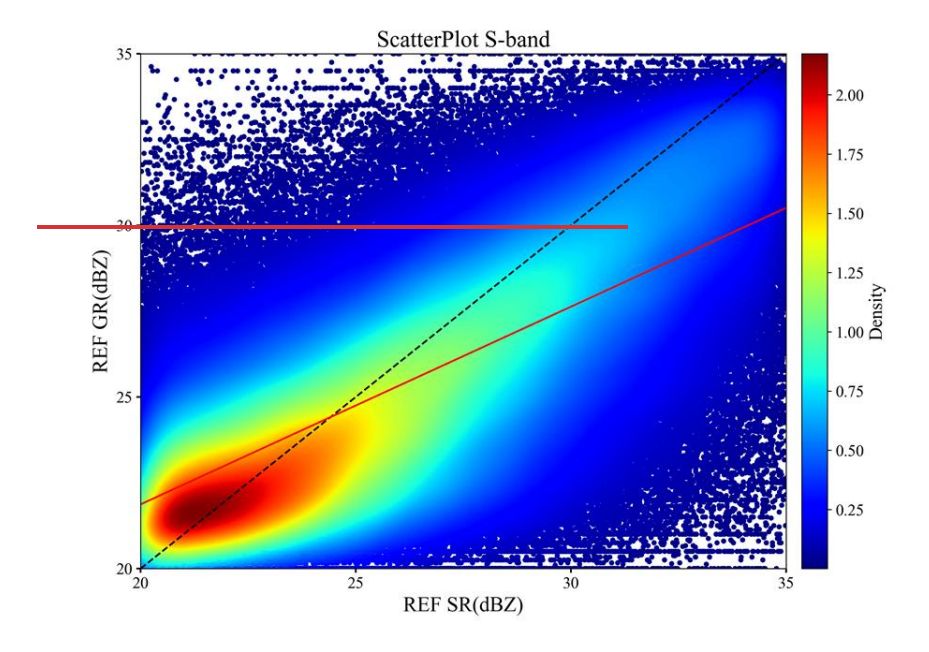


Figure 2324. Satellite -based consistency results of the SC modelmethod radar in Sanya City, Hainan Province, before and after rectification: left: before calibration; right: after calibration.

455

460

The FY-3G PMR Level 2 products have been available since January 2024. Due to the observational characteristics of polar-orbiting satellites, the orbital data over the South China region are limited. Conversely, the X-band phased-array weather radar provides high-frequency observations; however, due to the limited transmission bandwidth, the raw data frequency of the X-band phased-array radar is compressed from 1-minute intervals to 10-minute intervals, resulting in a smaller sample size for analysis. By analyzing the comparison results between the national S-band weather radars and the FY-3G PMR, it was found that the satellite's reflectivity factor is generally stronger, with a mean bias of 0.44 dB. This bias was not considered in the comparison of the results from the two modelmethods. If the satellite–ground consistency results are to be transferred to ground-based consistency results, then this bias needs to be removed.



带格式的: 缩进: 首行缩进: 0 字符

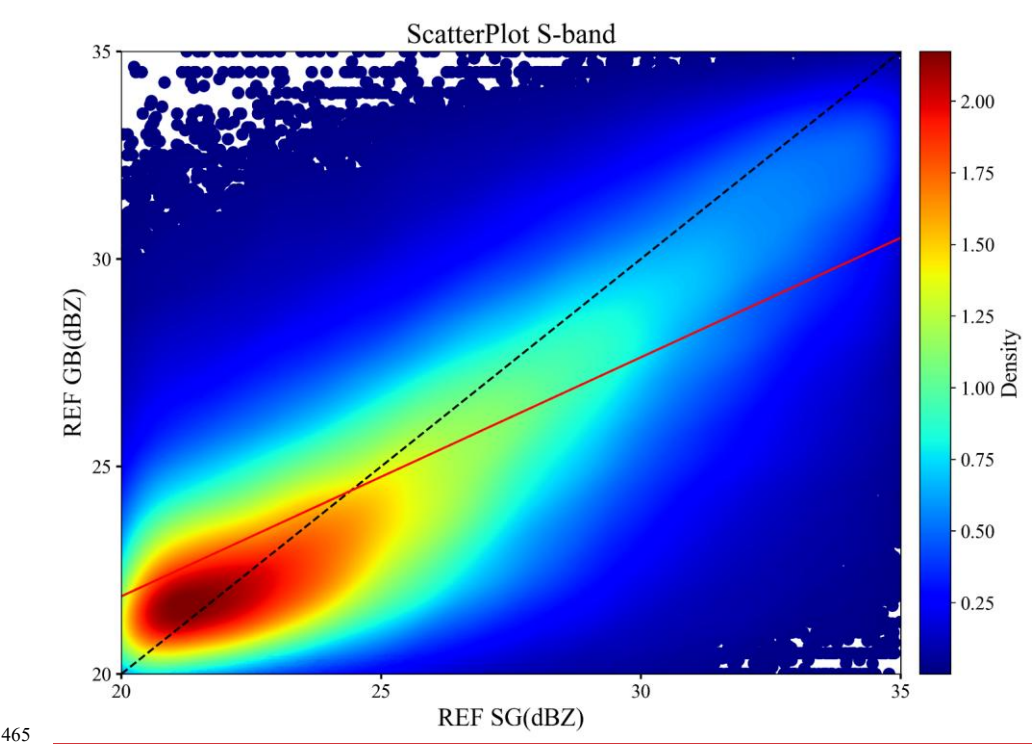


Figure 2425. Scatter distribution of satellite-ground consistency for S-band weather radars in China.

5. Conclusions

470

In conclusion, the two types of reflectivity factor comparison modelmethods can be used as calibration modelmethods for multi-band weather radars; however, there are also differences between them. Based on the analysis of precipitation events in 2024, it can be observed that the bias range between S-band weather radar and surrounding radars of the same band is relatively large. The absolute bias from satellite-to-ground analysis is smaller than that from ground-based analysis, while the standard deviation from satellite-to-ground analysis is larger than that from ground-based analysis, indicating greater dispersion in the bias between satellite and ground-based radars. The two analytical methods for the X-band phased array weather radar show good consistency and both demonstrate the significant attenuation characteristic of the X-band phased 475 array weather radar. Overall, the metrics from ground-based consistency analysis are greater than those from satellite-toground analysis, which may be due to the fact that the former considers data from the entire detection range, whereas the latter is limited by observation distance. This distance limitation eliminates the impact caused by inconsistencies in radar beam 带格式的: 缩进: 首行缩进: 2 字符

pointing calibration in the overlapping distant observation regions. More observational samples are needed for further analysis of this effect.

480

485

Appendix A: Weather Radar Hardware Information

设置了格式:字体:(中文)Times New Roman

The relevant hardware information for the 19 S-band weather radars and 13 X-band phased array radars used in this study is summarized in the table below. For the "Operation mode" column, we use the following numerical codes:

- 1. All-solid-state amplification
- 2. Amplification chain where a solid-state amplifier drives a klystron amplifier
- 3. Active phased array

<u>ID</u>	Band	Polarization type	<u>Doppler</u>	Operation	<u>Horizontal</u>	Antenna	Antenna	Reflectivity
			processing	mode	<u>beamwidth</u>	diameter	gain (dB)	range
			mode		<u>(°)</u>	<u>(m)</u>		
1	<u>S</u>	dual polarization	FFT	1	0.972	8.5	45.17	<u>≥460KM</u>
2	<u>S</u>	dual polarization	FFT	2	0.99	8.54	44.5	<u>≥460KM</u>
<u>3</u>	<u>S</u>	dual polarization	FFT	1	0.92	<u>8.5</u>	45.62	<u>≥460KM</u>
4	<u>S</u>	dual polarization	FFT	1	0.98	8.5	44.7	<u>≥460KM</u>
<u>5</u>	<u>S</u>	dual polarization	FFT	2	0.94	8.534	45.1	<u>≥460KM</u>
<u>6</u>	<u>S</u>	dual polarization	FFT	2	0.981	8.5	45.96	<u>≥460KM</u>
7	<u>S</u>	dual polarization	FFT	2	0.912	8.45	45.11	<u>≥460KM</u>
8	<u>S</u>	dual polarization	FFT	2	0.967	8.54	45.12	<u>≥460KM</u>
9	<u>S</u>	dual polarization	FFT	2	0.912	8.5	45.11	<u>≥460KM</u>
<u>10</u>	<u>S</u>	dual polarization	FFT	2	0.927	8.54	45.49	<u>≥460KM</u>
<u>11</u>	<u>S</u>	dual polarization	FFT	2	0.987	8.4	44.73	<u>≥460KM</u>
<u>12</u>	<u>S</u>	dual polarization	FFT	2	0.9	<u>8.534</u>	45.8	<u>≥460KM</u>

带格式的: 居中 格式化表格

<u>13</u>	<u>S</u>	dual polarization	FFT	2	0.987	8.5	45.99	<u>≥460KM</u>
<u>14</u>	<u>S</u>	dual polarization	FFT	2	0.97	8.5	45.6	<u>≥230KM</u>
<u>15</u>	<u>S</u>	dual polarization	FFT	2	0.95	8.5	44.53	<u>≥460KM</u>
<u>16</u>	<u>s</u>	dual polarization	FFT	1	0.916	8.534	<u>45.54</u>	<u>≥460KM</u>
<u>17</u>	<u>s</u>	dual polarization	FFT	2	0.879	8.534	<u>45.45</u>	≥460KM
<u>18</u>	<u>S</u>	dual polarization	FFT	2	0.97	8.5	44.79	<u>≥460KM</u>
<u>19</u>	<u>S</u>	dual polarization	FFT	2	0.99	8.534	45.24	<u>≥460KM</u>
<u>20</u>	X	dual polarization	FFT	3	0.972	0.7	<u>36</u>	<u>≥230KM</u>
<u>21</u>	X	dual polarization	FFT	3	0.972	0.7	<u>36</u>	<u>≥230KM</u>
<u>22</u>	X	dual polarization	FFT	3	0.972	0.7	<u>36</u>	<u>≥230KM</u>
<u>23</u>	X	dual polarization	FFT	3	0.972	0.7	<u>36</u>	<u>≥230KM</u>
<u>24</u>	X	dual polarization	FFT	3	0.972	0.7	<u>36</u>	<u>≥230KM</u>
<u>25</u>	X	dual polarization	FFT	3	0.972	0.7	<u>36</u>	<u>≥230KM</u>
<u>26</u>	X	dual polarization	FFT	3	0.972	0.7	<u>36</u>	<u>≥230KM</u>
<u>27</u>	X	dual polarization	FFT	3	0.972	0.7	<u>36</u>	<u>≥230KM</u>
<u>28</u>	X	dual polarization	FFT	3	0.972	0.7	<u>36</u>	<u>≥230KM</u>
<u>29</u>	X	dual polarization	FFT	3	0.972	0.72	<u>36</u>	<u>≥230KM</u>
<u>30</u>	X	dual polarization	FFT	3	0.972	0.72	<u>36</u>	<u>≥230KM</u>
<u>31</u>	X	dual polarization	FFT	3	0.972	1.3	<u>36</u>	<u>≥230KM</u>
<u>32</u>	X	dual polarization	FFT	3	0.972	0.72	<u>36</u>	<u>≥230KM</u>

带格式的: 缩进: 首行缩进: 0 字符

Author Contributions

H.H.: Conceptualization, Methodology, Formal analysis, Writing—original draft preparation, Writing—review and editing,

490 Supervision

S.P.: Conceptualization, Validation

L.W.: Data curation, Funding acquisition

N.S.: Project administration

C.Z.: Validation, Investigation

495 H.W.: Investigation, Validation

Y.L.: Resources, Supervision

References

505

2020.

Dinku, T., Anagnostou, E. N., Borga, M.:Improving radar-based estimation of rainfall over complex terrain. J. Appl. Meteor, 41(12):1163-117, 2002.

500 Liu Yunlei, Li Changxing, Zhang Lejian, Wen Hao, Wang Shudong.: Statistical analysis of terrain blockage impacts on the CINRAD network based on DEM data, Acta Meteorologica Sinica, 78(4):705-720, 2020.

Travis, D. J., & Carleton, A. M.: Radar beam pointing accuracy and its implications for precipitation estimation. J. Atmos. Oceanic. Technol., 55(3), 567-580,2016.

Lin Tang, Jian Zhang, Micheal Simpson, et al.: Updates on the Radar Data Quality Control in the MRMS Quantitative Precipitation Estimation System, J. Atmos. Oceanic. Technol. 1521-1537, DOI: https://doi.org/10.1175/JTECH-D-19-0165.1, 2020.

Zhang, G.: Weather Radar Polarimetry. CRC Press, 304 pp, 2017.

510 Smith, T. M., and Coauthors, Multi-Radar Multi-Sensor (MRMS) severe weather and aviation products: Initial operating capabilities, Bull. Amer. Meteor. Soc., 97, 1617-1630, https://doi.org/10.1175/BAMS-D-14-00173.1,2016.

Zhang, G.: Weather Radar Polarimetry, CRC Press, 304 pp, 2017.

Lin Tang, Jian Zhang, Micheal Simpson, et al.: Updates on the Radar Data Quality Control in the MRMS Quantitative Precipitation Estimation System, J. Atmos. Oceanic. Technol. 1521-1537, DOI: https://doi.org/10.1175/JTECH-D-19-0165.1,

Ryzhkov, A., and Zrnić, D. S.: Polarimetric rainfall estimation in the presence of anomalous propagation, J. Atmos. Oceanic Technol., 12(2), 229-244, doi: 10.1175/1520-0426(1995)012<0229:PREITP>2.0.CO;2., 1995.

Fabry, F., and Zawadzki, I.: Long-term radar observations of the melting layer of precipitation and their interpretation. Journal of the Atmospheric Sciences, 52(7), 838-851.DOI: 10.1175/1520-0469(1995)052<0838:LTROOT>2.0.CO;2, 1995.

设置了格式:字体:(中文)+中文正文(宋体),(中文)简体中文(中国

设置了格式:字体:(中文)+中文正文(宋体),(中文)简体中文(中国

- 520 Steiner, M., Houze, R. A., & Yuter, S. E.: Climatological characterization of three-dimensional storm structure from operational radar and rain gauge data. Journal of Applied Meteorology, 34(9), 1978-2007.DOI: 10.1175/1520-0450(1995)034<1978:CCOTDS>2.0.CO;2, 1995.
 - Bringi, V. N., and Chandrasekar, V.: Polarimetric Doppler Weather Radar: Principles and Applications. Cambridge University Press. DOI: 10.1017/CBO9780511541094,2001.
- 525 Gou, Y., H. Chen, and J. Zheng: An improved self-consistent approach to attenuation correction for C-band polarimetric radar measurements and its impact on quantitative precipitation estimation, Atmos. Res., 226, 32–48, 2019.
 Aart Overeem, Hylke de Vries, Hassan Al Sakka, Remko Uijlenhoet, and Hidde Leijnse: Rainfall-Induced Attenuation Correction for Two Operational Dual-Polarization C-Band Radars in the Netherlands, J. Atmos. Oceanic. Technol.,1125–
- 530 Gourley, J., Kaney, B., Maddox, R. A.: Evaluating the calibrations of radars: a software approach[C]//Proceedings of the 31st International Conference on Radar Meteorology. Seattle: American Meteorological Society: 459-462, 2003.

1142, DOI: https://doi.org/10.1175/JTECH-D-20-0113.1,2021.

- Smith, R., & Johnson, P.: Evaluation of radar data consistency and matching point quality in atmospheric studies. J. Atmos. Oceanic. Technol., 35(7), 1234-1248.https://doi.org/10.1175/JTECH-D-18-0012.1, 2018.
- Gao, J., Zhang, L., Zhang, H.: A robust algorithm for radar data consistency evaluation and quality control of matching points.
- 535 IEEE Transactions on Geoscience and Remote Sensing, 58(3), 1456-1468.https://doi.org/10.1109/TGRS.2019.2941234, 2020.
 Zhang, Z. Q. and Liu, L. P.: A simulation and analysis of the observation errors of cloud intensity and structure with the S-band phased array radar and the CINRAD/SA[J]. Acta. Meteor. Sin., 69(4): 729-735 (in Chinese),2011.
 - Vukovic, Z. R., Young, J. M. C., Donaldson, N.: Inter-radar comparison accounting for partially overlapping volumes[C]//Proceedings of the 8st European Conference on Radar in Meteorology and Hydrology. Germany: Garmisch-Partenkirchen, 2014.
 - Wu, C., Liu, L. P., Zhang, Z. Q.: Quantitative comparison algorithm between the S-band phased array radar and the CINRAD/SA and its preliminary application[J]. Acta Meteor Sin, 72(2): 390-401 (in Chinese), 2014.
- Zhang, L., Yang, H. P., Pei, C., et al. Analysis and application of the test method of reflectivity difference between adjacent radars[J]. Meteor Mon, 44(2): 268-276 (in Chinese), 2018.
 - Xiao, Y. J., Liu, L. P.: Study of methods for interpolating data from weather radar network to 3-D grid and mosaics[J]. Acta Meteor Sin, 64(5): 647-657 (in 402 Chinese)., 2006,
 - Ye, F., Liang, H. H., Wen, H., et al.: Research on homogeneity evaluation system of neighboring weather radars based on single-station CAPPI grid data[J]. Meteor Mon, 46(1): 50-62 (in Chinese), 2020.
- Lakshmanan, V., Hondl, K., Stumpf, G. J.: Quality control of weather radar data using texture features and a neural network, J. Atmos. Oceanic. Technol., 23(7), 1020-1031, https://doi.org/10.1175/JTECH1892.1,2006.
 - Wang J X, Wolff D B, et al.: Comparisons of reflectivities from the TRMM precipitation radar and ground-based radars. J. Atmos. Oceanic. Technol.,26(5):857-875,2009.

设置了格式:字体:(中文)+中文正文(宋体),(中文)简体中文(中国+肽)

设置了格式: 字体: (中文)+中文正文(宋体), (中文)简体中文(中国大陆)

 $Park \ S., Jung \ S. \ H., Lee \ G. \ Cross \ validation \ of \ TRMM \ PR \ reflectivity \ profiles \ using \ 3D \ reflectivity \ composite \ from \ the \ ground-park \ S.$

based radar network over the Korean Peninsula. J. Hydrometeor.,16(2):668-687, 2015.

Robert A. Warren, Alain Protat, Steven T. Siems & Hamish A. Ramsay, et al.: Calibrating Ground-Based Radars against

TRMM and GPM, J. Atmos. Oceanic. Technol., JTECH-D-17-0128.1.DOI:10.1175/JTECH-D-17-0128.1.,2018.

Alain Protat, Valentin Louf, Joshua Soderholm, Jordan Brook, William Ponsonby: Three-way Calibration Checks Using

 $\underline{Ground\text{-}Based, Ship\text{-}Based and Spaceborne Radars, Atmospheric Measurement Techniques, 15(4):915\text{-}926\text{,}2022\text{. }DOI}$

10.5194/amt-15-915-2022

Zhi Li, Yixin Wen, Liang Liao, et al.: Joint Collaboration on Comparing NOAA's Ground-Based Weather Radar and NASA–JAXA's Spaceborne Radar. BAMS, 104(8).DOI:10.1175/BAMS-D-22-0127.1.,2023.

He H Z, Cheng M H, Zhou K J, et al.: Comparison of data and product obtained by TRMM/PR and Hong Kong radar[J]. Meteor. Mon..28(10):32-36(in Chinese), 2002.

565 Zhai P M, Jia L, et a.: IConsistency evaluation for observation and TRMM precipitation estimation in Tibetan Plateau[J].Meteor. Mon.,41(9):1119-1125(in Chinese), 2015.

Wang Z H, Li S Y, Dai J H, et al.: Comparative case study on the observations between the space-borne radar and ground-based radar. Plateau Meteor, 34(3): 804-814 (in Chinese), 2015.

Bolen, S. M., & Chandrasekar, V.: Quantitative cross-validation of space-based and ground-based radar observations. Journal

of Applied Meteorology, 42(4),502525,

580

https://doi.org/10.1175/15200450(2003)042<0502:QCVOSB>2.0.CO;2, 2003.

Schwaller, M. R., & Morris, K. R.: A ground validation network for the Global Precipitation Measurement Mission. Journal of Atmospheric and Oceanic Technology, 28(3), 301-319. https://doi.org/10.1175/2010JTECHA1403.1,2011.

China Meteorological Administration. The FY-3G satellite: Advancing precipitation measurement with Ku and Ka band radars.

Journal of Satellite Meteorology and Remote Sensing, 12(4), 123-135, 2023.

Wu Qiong: Fengyun-3 (Batch 03) Meteorological Satellite Ground Application System Project G Satellite Precipitation Measurement Radar KuR Product User Manual, National Satellite Meteorological Center.1-26,2023(a).

Wu Qiong, Yang Meilin, Chen Lin, Yin Honggang, Shang Jian, Gu Songyan. A frequency correction algorithm for spaceborne precipitation measurement radar and ground-based weather radar. Acta Meteorologica Sinica, 81(2):353-360, 2023(b).

National Weather Service, Ground-based weather radar mode-switching trials: An overview of VCP11, VCP21, and VCP31 modes. Journal of Weather Radar Technology and Applications, 18(1), 45-53, 2025.

Yang Hongping, Han Wei, Wang Hui, Hu Heng.: A Reference Positioning Methodology for Computing Geodetic Coordinates of Radar Echo. Meteorological Science and Technology, 51(1), 22-30, 2023.

Yu, Xiaoding. Principles and Operational Applications of Doppler Weather Radar. Meteorological Press, Beijing, 2007.

585 Lu D.J., Hu H., Wu L. et al.: Influence factors analysis and improvement of consistency evaluation algorithm between weather radar. Meteor. Mon., 50(4):475-487(in Chinese), 2024. 设置了格式: 字体: (中文) Times New Roman

设置了格式:字体:(中文)+中文正文(宋体),(中文)简体中文(中国 大陆)

设置了格式: 非突出显示

- Maddox, R. A., Zhang, J., Gourley, J. J., & Howard, K. W.: Weather radar coverage over the contiguous United States. Weather and Forecasting, 17(4), 927-934. https://doi.org/10.1175/1520-0434(2002)017<0927:WRCOOT>2.0.CO;2, 2002.
- Bech, J., Codina, B., Lorente, J., & Bebbington, D.: The sensitivity of single polarization weather radar beam blockage correction to variability in the vertical refractivity gradient. J. Atmos. Oceanic Technol., 20(6), 845-855. https://doi.org/10.1175/1520-0426(2003)020<0845:TSOSPW>2.0.CO;2., 2003.
 - Biggerstaff M I, Listenmaa A.: An improved scheme for convective/stratiform echo classification using radar reflectivity. J.Appl.Meteor.,39:2129~2150, 2000.
 - Xiao Yanjiao and Liu Liping: Identification of Stratiform and Convective Cloud Using 3D Radar Reflectivity Data. Chinese Journal of Atmospheric Sciences, 31(4):645-654, 2007.
 - Xiao, Yanjiao, Ma, Zhongyuan, & Li, Zhonghua. Improved algorithms for radar echo top height, vertically integrated liquid water content, and its density. Torrential Rain and Disasters, 2009(03): 20–24. DOI:10.3969/j.issn.1004-9045.2009.03.003.

 Testud, J., Le Bouar, E., Obligis, E., & Ali-Mehenni, M., "The rain profiling algorithm applied to polarimetric weather radar."

 J. Atmos. Oceanic Technol., 17(3), 332–356,2000.(a),
- 600 Testud, J., Oury, S., Black, R. A., Amayenc, P., Dou, X.:The concept of "normalized" distribution to describe raindrop spectra: A tool to analyze and parameterize radar rainfall relationships. Journal of Applied Meteorology, 39(5), 761-774, https://doi.org/10.1175/1520-0450(2000)039<0761:TCONDT>2.0.CO;2,2000.(b)
 - Bringi, V. N., & Chandrasekar, V.: Polarimetric Doppler Weather Radar: Principles and Applications. Cambridge University Press., https://doi.org/10.1016/j.atmosres.2019.03.006. 2001.
- 605 Melsheimer, C., & Coifman, B.: Analysis of sea clutter in weather radar observations. J. Atmos. Oceanic Technol., 15(5), 1225-1238, https://doi.org/10.1175/1520-0426(1998)015<1225:AOSCIW>2.0.CO;2,1998.
 - Skolnik, M. I.: Radar Handbook (3rd ed.). McGraw-Hill Education, 2008.
 - Kitchen, M., and Jackson, P. M.: Weather radar performance at long range—Simulated and observed. J. Atmos. Oceanic Technol., 10(5), 819-832, https://doi.org/10.1175/1520-0426(1993)010<0819:WRPALR>2.0.CO;2,1993.
- 610 Doviak, R. J., and Zrnić, D. S.: Doppler Radar and Weather Observations (2nd ed.). Academic Press. 2006.
 - Holleman, I., and Beekhuis, H.: Analysis and correction of dual PRF velocity data. J. Atmos. Oceanic Technol., 21(3), 429-442, https://doi.org/10.1175/1520-0426(2004)021<0429:AACODP>2.0.CO;2,2004.
 - Saltikoff, E., Huuskonen, A., Holleman, I., et al.: The threat to weather radars by wireless technology. Bulletin of the American Meteorological Society, 97(7), 1159-1167, https://doi.org/10.1175/BAMS-D-15-00048.1,2016.
- 615 Nguyen, L., & Chandrasekar, V.: Spectrum-based signal processing for weather radar interference mitigation. IEEE Transactions on Geoscience and Remote Sensing, 55(5), 2835-2845.https://doi.org/10.1109/TGRS.2017.2654500, 2017.
 - Wen Hao, Zhang Lejian, Liang Haihe, Zhang Yang, "Radial interference echo identification algorithm based on fuzzy logic for weather radar." Acta Meteorologica Sinica, 78(1): 116-127,2020.(In Chinese)
 - Xiao LS, Hu DM, Chen S, et al., 2021. Study on attenuation correction algorithm of X-band dual polarization phased array
- fadar [J]. Meteorological Monthly, 47(6): 703 716 (in Chinese).

设置了格式: 字体: (中文) +中文正文(宋体), (中文) 简体中文(中国 大陆)

设置了格式: 字体: (中文) +中文正文(宋体), (中文)简体中文(中国大陆)

Holleman, I; Huuskonen, A and Taylor, B: Solar Monitoring of the NEXRAD WSR-88D Network Using Operational Scan Data, 39 (2), J. Atmos. Oceanic Technol., pp.193-205. https://doi.org/10.1175/JTECH-D-20-0204.1, 2022. Hubbert, J. C., & Bringi, V. N.: The effects of miscalibration on polarimetric radar parameters. J. Atmos. Oceanic Technol., 17(1), 51–64, 2000.

A. Peng, W. Liu, Y. Zuo and L. Guo, Calibrator Irregularity Error Compensation for Radar Cross Section Measurement, JEEE
Antennas and Wireless Propagation Letters, 21(6), 1263-1267, doi: 10.1109/LAWP.2022.3163910. 2022. Travis, D. J., & Carleton, A. M.: Radar beam pointing accuracy and its implications for precipitation estimation. J. Atmos. Oceanic. Technol., 55(3), 567-580,2016.

设置了格式: 字体: 非倾斜